Hierarchically decomposed finite element method for a triply coupled piezoelectric, structure, and fluid fields of a thin piezoelectric bimorph in fluid

Prakasha Chigahalli Ramegowda, Daisuke Ishihara*, Rei Takata, Tomoya Niho, Tomoyoshi Horie

Department of Intelligent and Control Systems,
Kyushu Institute of Technology, 680-4 Kawazu, Iizuka, Fukuoka, 820-8502, Japan

Abstract

This paper proposes a numerical method for analyzing a thin piezoelectric bimorph in fluid. A hierarchically decomposed finite element method (FEM) is proposed for modeling the triply coupled piezoelectric-structure-fluid interaction. The electromechanical coupling (piezoelectric-structure interaction) behavior in a thin piezoelectric bimorph is described by the classical constitutive equation, the incompressible fluid flows by the Navier-Stokes equation and the structure by the Cauchy equation of motion. The piezoelectric-structure-fluid interaction system is decomposed into subsystems of fluid-structure interaction (FSI) and piezoelectric field, then the piezoelectric field and the FSI are coupled using the block Gauss-Seidel method, the fluid-structure interaction is split into the fluid-structure velocity field and the pressure field using an algebraic splitting and the fluid-structure velocity field is partitioned into fluid velocity field and structure velocity field. Using the proposed method, the resonance characteristics of a piezoelectric bimorph cantilever made of PVDF and PZT-5H material in fluid are investigated for actuation and sensor configurations.

Keywords: Hierarchical decomposition, piezoelectricity, finite element method (FEM), piezoelectric-structure interaction, Fluid-structure interaction (FSI), thin piezoelectric bimorph.

1. Introduction

Thin piezoelectric bimorph devices are widely used in actuation and sensing applications. During recent years, the flexible wings of insect-like micro air vehicles [1, 2] are actuated by a thin piezoelectric bimorph actuator. These actuators can produce large deformations when operated near resonance. The piezoelectric actuation amplitude is damped significantly due to the fluid force from the surrounding fluid media. Therefore, it is important to consider the analysis of a thin piezoelectric bimorph actuator in fluid. Also, over recent years, with the rise in

---

*Corresponding author
   Email addresses: `prakasha@solid.mse.kyutech.ac.jp` (Prakasha Chigahalli Ramegowda),
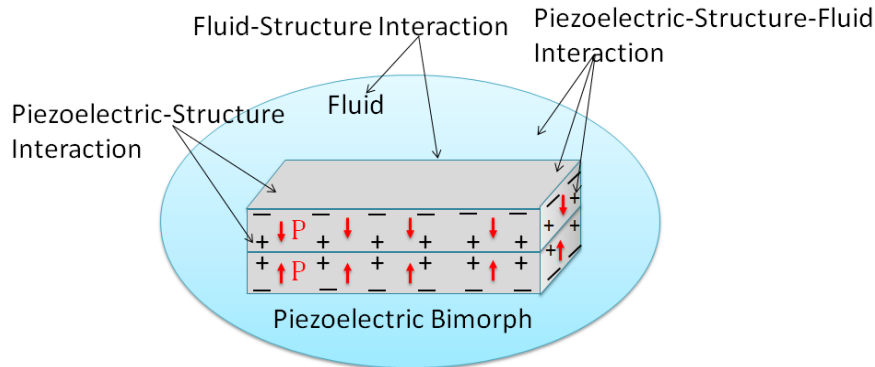`ishihara@mse.kyutech.ac.jp` (Daisuke Ishihara*)

Fig. 1. Schematic representation of a piezoelectric bimorph in fluid

the demand of energy has attracted significant research interest in energy harvesting describing the process of generating electrical energy from external sources in the surroundings, such as structural mechanical vibrations, ocean waves, wind flow and many. The energy harvesting using thin piezoelectric bimorph devices converts mechanical energy such as ocean wave to the electric energy has attracted greater attention as a next electric generation system due to their strong electromechanical convertible characteristics. In piezoelectric energy harvesting applications, the sensor function of a thin piezoelectric bimorph is utilized [3–5]. In these applications, the large deformation of a thin piezoelectric bimorph device causes a strong interaction with the electric field (piezoelectric effect) and the surrounding fluid, and inversely, these two fields significantly affect the structural behavior of thin piezoelectric bimorph. This interdisciplinary coupling effect among the electric field, the surrounding fluid media, and the thin structure are very significant. Therefore, the triply coupled multiphysics analysis of piezoelectric, structure, and fluids is very important. Fig. 1 shows the schematic representation of a piezoelectric bimorph in fluid and physical domain interaction.

The analytical solutions to the model equations of piezoelectric-structure-fluid interaction systems are limited in the scope and their simulation is a difficult task. The triply coupled phenomenon of the piezoelectric-structure-fluid interaction system for a piezoelectric bimorph in fluid using FEM has gained a popular research interest in the last couple of years due to the significant engineering applications, see for example, refs. [5, 6]. In the study of the piezoelectric-structure-fluid interaction, numerical simulations are very effective since they are appropriate for parametric studies, detailed analysis and thorough understanding of coupled dependencies, and reduce the need for experimental studies. So this work is focused on the development of the finite element method for the piezoelectric-structure-fluid interaction of a thin piezoelectric bimorph in fluid.

The application of numerical methods to the solution of a coupled problems is generally solved using either a monolithic or a partitioned approach. A monolithic solution scheme treats all the domains simultaneously, leading to a single set of algebraic equations and solved in a single mathematical framework. Monolithic approaches are generally known to be robust, accurate and strongly coupled. However, the monolithic approaches are computationally very expensive and a monolithic FSI formulation can lead to an ill-conditioned equation system. In contrast to a monolithic approach, a partitioned approach treats each physical field as a separate entity, discretized and numerically solved, and they are coupled via exchanging the variable between

each subsystem. The partitioned approaches are easy for the implementation, enabling the reuse of already developed existing codes (modularity), and are appropriate for parallel computation. Monolithic electromechanical coupling and monolithic FSI system can be found respectively in refs. [7–9] and [10–12]. Some of the partitioned iterative approaches to solving piezoelectric-structure interaction in a piezoelectric continuum are given in [13–17]. Similarly, for the FSI system, partitioned simulation strategies can be found in refs. [18–21].

Several algorithms have been proposed for solving electrostatic-fluid-structure interaction problems, see for example, refs. [22–26]. Rochus et al. [22], De et al. [23], and Ghosh at al [24] have proposed a monolithic approach while Ishihara et al. [25] proposed a hierarchal decomposition method and Raulli [26] proposed a partitioned approach to analyzing the Reynolds squeeze film damping effect between the structure and fluid domains where the structure is driven vertically by electrostatic actuation. The electrostatic actuation is completely different from the direct and inverse piezoelectric effect in-terms of constitutive equations. Above mentioned studies cannot solve electromechanical coupling in the piezoelectric materials. Direct and inverse piezoelectric equations are much more complicated than electrostatic actuation. One-way coupling between piezoelectric-structure and fluid-structure interactions can be found in [27, 28]. These one way coupling method is used for piezoelectrically actuated structure incorporating the effect of fluid damping. However, they can not be used for the direct piezoelectric effect incorporating fluid and structure effects. Bathe et al. [29] had proposed an FE solution method for electromagnetics with fluid flows and structures. Again, the electromagnetic effect is different from the piezoelectric effect. A few research works on the triply coupled finite element analysis piezoelectric-structure-fluid interaction system can be found in [5, 6].

Ravi et al. [5] had proposed a monolithic approach to solve piezoelectric- fluid-structure interaction of a piezoelectric bimorph beam driven by fluid flow. Although the monolithic approach is strongly coupled by the formulation itself, but are computationally expensive and lead to ill-conditioned monolithic system [21]. Kaneko et al. [6] had proposed a simple staggered iterative approach and employed the 2D solid elements to analyze the direct and inverse piezoelectric effect. Using a staggered iterative method they connected the fluid, structure, and piezoelectric solvers. The detailed finite element coupled strategy for the EFSI system is not provided and not investigated in [6]. In [5, 6], they used solid elements to analyze both the direct and inverse piezoelectric effect in a thin piezoelectric bimorph. However, solid elements employed therein are inappropriate for the discretization of thin structures and also they are expensive computationally. On the other hand, in our previous study [15], we proposed a novel FE method to analyze piezoelectric-structure interaction of a thin piezoelectric bimorph using solid element for piezoelectric analysis and shell for thin structure analysis to overcome the drawbacks of using a same finite element for electromechanical coupled analysis of a thin piezoelectric devices [30].

In the present study, the piezoelectric-structure-fluid interaction is hierarchically decomposed. Ishihara et al. [25] proposed a hierarchal decomposition method to solve electrostatic-fluid-structure interaction which is completely different from piezoelectric-fluid-structure interaction except for FSI analysis. In the proposed method, the piezoelectric-structure-fluid interaction system is decomposed into subsystems of fluid-structure interaction (FSI) and piezoelectric field, then the piezoelectric field and the fluid-structure interaction are coupled using the block Gauss-Seidel method, the fluid-structure interaction is split into the fluid-structure velocity field and the pressure field using an algebraic splitting or projection method for the FSI system [31], and the fluid-structure velocity field is partitioned into fluid velocity field and structure velocity field.

The combination of the Lagrangian and Eulerian description, respectively, for the structure

and fluid mechanics, known as arbitrary Lagrangian-Eulerian (ALE) description [32] is used in the present formulation. When the problem is geometrically nonlinear, full Newton-Raphson (N-R) iterations are performed for the structural part. The authors study two approaches for the management of the BGS and N-R loops, similar to that shown in [15]. In the first approach, non-linear N-R loop is placed inside the BGS iteration loop. In this approach, in every BGS iteration, there are several N-R iterations are executed until the energy tolerance criteria is satisfied. On the other hand, in the second approach, the BGS and N-R loops are unified into a single loop. Therefore, we call this approach as unified BGS and NR loops. In this approach, the number of BGS iterations and N-R iterations are the same. These approaches are intended to study the computational efficiency of the proposed method.

The proposed strongly coupled hierarchically decomposed method for triply coupled piezo-electric, structural, and fluid fields of thin piezoelectric bimorph in fluid is applied to a flexible restrictor flap in the converging channel [33], where the rubber flap is replaced by the piezoelectric bimorphs made of PVDF or PZT5H. Three electric configurations of piezoelectric bimorph (actuator setup, closed-circuit sensor setup, and open-circuit sensor setup) along with the inlet fluid velocity boundary condition in converging channel as defined in [31, 33] are studied. The resonance frequency of the piezoelectric bimorph actuator analysis in fluid agrees well with the theoretical and numerical pure FSI cases. The tendency of the open circuit and closed circuit sensor frequency for PVD and PZT-5H piezoelectric bimorphs show the same tendency with the present state of the survey and theoretical approximations.

2. Governing Equations

2.1. Piezoelectricity

Piezoelectricity is basically the interaction between the electrical and mechanical states in a piezoelectric material. It can be subdivided into the direct piezoelectric effect (sensor effect) and the inverse piezoelectric effect (actuator effect). The mechanical part is solved using the equilibrium equation of the structure and the electric part is solved using Maxwell's equation of equilibrium for the quasi-static electric field. The constitutive equations of linear piezoelectricity can be written as

$$\sigma_{ij} = C_{ijkl}^E S_{kl} - e_{kij}E_k, \tag{1}$$
$$D_i = e_{ikl}S_{kl} + \varepsilon_{ik}^S E_k, \tag{2}$$

where σ_{ij} is the stress tensor, C_{ijkl}^E is the elastic constitutive tensor, S_{kl} the mechanical strain tensor, e_{kij} the piezoelectric coupling coefficient, E_k the electric field vector, and ε_{ik}^S the dielectric permittivity tensor. The superscripts E and S denote that the elastic constants and the dielectric constants are evaluated at a constant electric field and a constant strain, respectively.

In the linear piezoelectric analysis, the mechanical strain tensor S_{ij} and the mechanical displacement vector u_i are related as

$$S_{ij} = \frac{1}{2}(u_{i,j} + u_{j,i}). \tag{3}$$

The electric field vector E_i and the scalar electric potential $\phi_{,i}$ are related as

$$E_i = -\phi_{,i}. \tag{4}$$

The essential and natural boundary conditions related to the electrical filed are written as

$$\phi = \bar{\phi}, \tag{5}$$

$$D_i n_i = \bar{q}, \tag{6}$$

where $\bar{\phi}$ and $\bar{q}$ are the prescribed electric potential and surface charge on the piezoelectric boundary corresponding to the Dirichlet- and Neumann-type, respectively, and n_i is the outward unit normal vector.

2.2. Structure

The equilibrium equation of the structure can be written as

$$\rho^{\mathrm{s}} \frac{\mathrm{d}^2 u_i^{\mathrm{s}}}{\mathrm{d}t^2} = \frac{\partial \sigma_{ji}^{\mathrm{s}}}{\partial x_j} + \rho^{\mathrm{s}} g_i^{\mathrm{s}}, \quad \text{in } {}^t\Omega^{\mathrm{s}}, \tag{7}$$

where ${}^t\Omega^{\mathrm{s}}$ is the spatial domain of a structure at time t, ρ^{s} is the density of the structure, u_i^{s} is the structural displacement vector, $\frac{\mathrm{d}}{\mathrm{d}t}$ is the so-called material derivative, g_i^{s} is the body force vector acting on the structure, and σ_{ij}^{s} is the 2nd Piola-Kirchhoff stress tensor. While the structure undergoes large deformations causing to geometric nonlinearities, the strains are assumed to be small, thus a materially linear elastic model is assumed. Here, we use 2nd Piola-Kirchhoff stress tensor and Green-Lagrange strain tensor in total Lagrangian formulation. For the elastic body, the Dirichlet- and Neumann-type boundary conditions are given by

$$v_i^{\mathrm{s}} = \bar{v}_i^{\mathrm{s}}, \quad \text{on } \Gamma_{\mathrm{E}}^{\mathrm{s}}, \tag{8}$$

$$\sigma_{ij}^{\mathrm{s}} . n_j^{\mathrm{s}} = \tau_i^{\mathrm{s}}, \quad \text{on } \Gamma_{\mathrm{N}}^{\mathrm{s}}. \tag{9}$$

where $\Gamma_{\mathrm{E}}^{\mathrm{s}}$ and $\Gamma_{\mathrm{N}}^{\mathrm{s}}$ are complementary subsets of ${}^t\Gamma^{\mathrm{f}}$ corresponding to the Dirichlet- and Neumann-type boundary conditions at time t, $\bar{v}_i^{\mathrm{s}}$ and τ_i^{s} are the prescribed structure velocity and traction values on the complementary subset of ${}^t\Gamma^{\mathrm{s}}$.

2.3. Fluid

Let the fluid be an incompressible viscous Newtonian fluid. The fluid flow is governed by the Navier-Stokes equations for an incompressible fluid. The arbitrary Lagrangian-Eulerian formulation is employed to describe the incompressible viscous fluid motion in the deformable domain. The ALE description of the incompressible Navier-Stokes equations as the governing equations of the fluid motion [32]:

$$\rho^{\mathrm{f}} \frac{\partial v_i^{\mathrm{f}}}{\partial t} + \rho^{\mathrm{f}} (v_j^{\mathrm{f}} - \hat{v}_j^{\mathrm{f}}) \frac{\partial v_i^{\mathrm{f}}}{\partial x_j} = \frac{\partial \sigma_{ji}^{\mathrm{f}}}{\partial x_j} + \rho^{\mathrm{f}} g_i^{\mathrm{f}}, \quad \text{in } {}^t\Omega^{\mathrm{f}}, \tag{10}$$

under the incompressibility constraint

$$\frac{\partial v_i^{\mathrm{f}}}{\partial x_i} = 0, \quad \text{in } {}^t\Omega^{\mathrm{f}}, \tag{11}$$

where the superscript f indicates the fluid components, ${}^t\Omega^{\mathrm{f}}$ is the spatial fluid domain at time t, ρ^{f} is the density of the fluid, v_i^{f} is the fluid velocity vector, $\hat{v}_i^{\mathrm{f}}$ is the velocity vector of the mesh

deformation in the ALE co-ordinate, g_i^{f} is the body force vector acting on the fluid, and σ_{ij}^{f} is the stress tensor of the fluid. To solve for the equilibrium fluid equation Eq.(10), one has to specify the essential and natural boundary conditions on the closed boundary of the fluid domain $^{t}\Gamma^{\mathrm{f}}$. The essential or Dirichlet and the natural or Neumann boundary conditions could be imposed at different segments of the boundary $^{t}\Gamma^{\mathrm{f}}$:

$$v_i^{\mathrm{f}} = \bar{v}_i^{\mathrm{f}}, \quad \text{on } \Gamma_{\mathrm{E}}^{\mathrm{f}}, \tag{12}$$
$$\sigma_{ij}^{\mathrm{f}}.n_j^{\mathrm{f}} = \tau_i^{\mathrm{f}}, \quad \text{on } \Gamma_{\mathrm{N}}^{\mathrm{f}}, \tag{13}$$

where $\Gamma_{\mathrm{E}}^{\mathrm{f}}$ and $\Gamma_{\mathrm{N}}^{\mathrm{f}}$ are complementary subsets of $^{t}\Gamma^{\mathrm{f}}$ corresponding to the Dirichlet- and Neumann-type boundary conditions at time t, $\bar{v}_i^{\mathrm{f}}$ and τ_i^{f} are the prescribed fluid velocity and traction values on the complementary subset of $^{t}\Gamma^{\mathrm{f}}$.

2.4. Interface conditions

The interaction conditions on the interface between the fluid and the structure are imposed using the following geometric compatibility and equilibrium conditions:

$$v_i^{\mathrm{f}} = v_i^{\mathrm{s}} \equiv v_i^{\mathrm{fs}}, \quad \text{on } \Gamma^{\mathrm{fs}}, \tag{14}$$
$$\sigma_{ij}^{\mathrm{f}}.n_j^{\mathrm{f}} + \sigma_{ij}^{\mathrm{s}}.n_j^{\mathrm{s}} = \tau_i^{fs}, \quad \text{on } \Gamma^{\mathrm{fs}}, \tag{15}$$

where the superscript fs indicates the components of the fluid-structure interface, v_i^{fs} is the fluid-structure interface velocity vector, and τ_i^{fs} is the surface force vector acting on the fluid-structure interface.

3. Finite Element Formulation

3.1. Piezoelectric-Structure Interaction

Applying finite element discretization to Eqs.(1) and (2), the following coupled piezoelectric-structure system in the global coordinates can be obtained in matrix form [7, 9, 14]:

$$\mathbf{Ma} + \mathbf{Ku} + \mathbf{K}_{\mathrm{u}\phi}\phi = \mathbf{g}, \tag{16}$$
$$\mathbf{K}_{\phi\phi}\phi + \mathbf{K}_{\phi\mathrm{u}}\mathbf{u} = \mathbf{q}, \tag{17}$$

where $\mathbf{M}$ is the mass matrix, $\mathbf{K}$ is the mechanical stiffness matrix of the piezoelectric material, $\mathbf{K}_{\phi\phi}$ is the dielectric stiffness matrix of the piezoelectric material, $\mathbf{K}_{\mathrm{u}\phi}$ is the piezoelectric coupling coefficient matrix of the piezoelectric material, $\mathbf{K}_{\phi\mathrm{u}}$ is the transpose of $\mathbf{K}_{\mathrm{u}\phi}$, $\mathbf{a}$ is the vector of the accelerations, $\mathbf{u}$ is the vector of the mechanical displacements, ϕ is the vector of electric potentials, $\mathbf{g}$ is the vector of the external mechanical forces, and $\mathbf{q}$ represents the vector of the external surface density charges on the piezoelectric material.

In the present work, the piezoelectric field (electric field) is solved using the 3D solid elements and the structure is solved using the shell elements (see [15]). Hence, Eqs.(16) and (17) can be written as

$$\text{Inverse piezoelectric effect using shell}: \quad \mathbf{M}^{\mathrm{s}}\mathbf{a}^{\mathrm{s}} + \mathbf{K}^{\mathrm{s}}\mathbf{u}^{\mathrm{s}} = \mathbf{g}^{\mathrm{s}} + {}_{\mathrm{e}}\mathbf{g}^{\mathrm{s}}, \tag{18}$$
$$\text{Direct piezoelectric effect using 3D solid}: \quad \mathbf{K}_{\phi\phi}\phi_{\mathrm{solid}} = \mathbf{q} + {}_{\mathrm{e}}\mathbf{q}_{\mathrm{solid}}. \tag{19}$$

In the above equations, the term $_e\mathbf{g}^s$ is the vector of the electrical forces generated in the piezo-electric material due to the inverse piezoelectric effect and $_e\mathbf{q}_{solid}$ is the vector of the induced electric charge due to the direct piezoelectric effect defined respectively as:

$$_e\mathbf{g}^s = {}_e\mathbf{T} \, _e\mathbf{g}_{solid}, \tag{20}$$

$$_e\mathbf{q}_{solid} = -\mathbf{K}_{\phi u}\mathbf{u}_{solid}, \tag{21}$$

where

$$_e\mathbf{g}_{solid} = -\mathbf{K}_{u\phi}\phi_{solid}, \tag{22}$$

$$\mathbf{u}_{solid} = {}_u\mathbf{T} \, \mathbf{u}^s. \tag{23}$$

The dielectric stiffness matrix $\mathbf{K}_{\phi\phi}$, the piezoelectric coupling coefficient matrix $\mathbf{K}_{u\phi}$ and its transpose $\mathbf{K}_{\phi u}$, the electric potential vector ϕ_{solid}, the vector of the induced electric charge $_e\mathbf{q}_{solid}$ due to the piezoelectric effect that are evaluated using the 3D solid elements. The displacements at the solid elements $\mathbf{u}_{solid}$ are obtained from the displacement transformation Eq.(23) using the displacements of the shell elements $\mathbf{u}^s$. In Eqs.(20) and (23), $_e\mathbf{T}$ and $_u\mathbf{T}$ are the force transformation matrix and displacement transformation matrix, respectively. The coupling between piezoelectric and structure fields is done by exchanging the variables using the block Gauss-Seidel method.

3.2. Fluid-Structure Interaction
3.2.1. Structure

Finite element spatial discretization to Eq.(7) using the shell element, we obtain the equilibrium equation for the structure in matrix form as

$$\mathbf{Q}^s \equiv {}_L\mathbf{M}^s\mathbf{a}^s + \mathbf{q}^s(\mathbf{u}^s) = \mathbf{g}^s, \tag{24}$$

where $\mathbf{M}^s$ is the mass matrix of the structure, $\mathbf{q}^s$ is the internal force vector, $\mathbf{a}^s$ is the acceleration vector of the structure, $\mathbf{u}^s$ is the displacement vector of the structure, $\mathbf{g}^s$ is the external force vector applied to the structure, $\mathbf{Q}^s$ is the equivalent internal force vector including all effects of the structure.

3.2.2. Fluid

Finite element spatial discretization to the incompressible Navier-Stokes Eqs.(10) and (11) can be written in matrix form, respectively, as

$$\mathbf{Q}^f \equiv {}_L\mathbf{M}^f\mathbf{a}^f + \mathbf{N}^f + \mathbf{C}^f\mathbf{v}^f - \mathbf{G}^f\mathbf{p}^f = \mathbf{g}^f, \tag{25}$$

$$_T\mathbf{G}^f\mathbf{v}^f = \mathbf{0}, \tag{26}$$

where $\mathbf{M}^f$ is the mass matrix of the fluid, $\mathbf{N}^f$ is the convective term vector of the fluid, $\mathbf{C}^f$ is the diffusion matrix of the fluid, $\mathbf{G}^f$ is the divergence operator matrix of the fluid, $\mathbf{a}^f$ is the acceleration vector of the fluid, $\mathbf{v}^f$ is the velocity vector of the fluid, $\mathbf{p}^f$ is the pressure vector of the fluid, $\mathbf{g}^f$ is the external force vector acting on the fluid, $\mathbf{Q}^f$ is the equivalent internal force vector including all effects of the fluid, the subscript L stands for lumping of the matrix, and the subscript T stands for transpose of the matrix. In the ALE formulation, the fluid convective term $\mathbf{N}^f$ is expressed as $\mathbf{N}^f(\mathbf{v}^f - \hat{\mathbf{v}}^f)\mathbf{v}^f$. In this study, a linear equal order interpolation velocity pressure element [34] is used for the incompressible fluid analysis. The stabilization formulations streamline-upwind/Petrov-Galerkin (SUPG) [35] and the pressure-stabilizing/Petrov-Galerkin (PSPG) [34, 36] for incompressible flows are adopted to avoid the numerical instabilities due to the fluid convection and the P1P1 elements.

7

3.2.3. Fluid-Structure Interaction

The geometric compatibility condition Eq.(14) and the equilibrium condition Eq.(15) on the fluid-structure interaction can be written in vector form, respectively, as

$$\mathbf{v}_c^{fs} \equiv \mathbf{v}_c^f = \mathbf{v}_c^s, \tag{27}$$

and

$$\mathbf{Q}_c^f + \mathbf{Q}_c^s = \mathbf{g}_c^{fs}. \tag{28}$$

Eqs. (24)–(26) are combined using the coupled conditions Eqs.(27) and (28) to form the monolithic equations as [31]

$$\mathbf{Q} \equiv {}_L\mathbf{M}\mathbf{a} + \mathbf{C}\mathbf{v} + \mathbf{N} + \mathbf{q}(\mathbf{u}) - \mathbf{G}\mathbf{p} = \mathbf{g}, \tag{29}$$

$$_T\mathbf{G}\mathbf{v} = 0. \tag{30}$$

The definitions of each of the matrices and the vectors appearing in Eqs.(29) and (30) are defined as

$$_L\mathbf{M} \equiv \begin{bmatrix} {}_L\mathbf{M}_{dd}^f & 0 & 0 \\ 0 & {}_L\mathbf{M}_{cc}^{fs} & 0 \\ 0 & 0 & {}_L\mathbf{M}_{dd}^s \end{bmatrix}, \tag{31a}$$

$$\mathbf{C} \equiv \begin{bmatrix} \mathbf{C}_{dd}^f & \mathbf{C}_{dc}^f & 0 \\ \mathbf{C}_{cd}^f & \mathbf{C}_{cc}^f & 0 \\ 0 & 0 & \mathbf{C}_{dd}^s \end{bmatrix}, \tag{31b}$$

$$\mathbf{G} \equiv \begin{bmatrix} \mathbf{G}_d^f \\ \mathbf{G}_c^f \\ 0 \end{bmatrix}, \tag{31c}$$

$$\mathbf{q}(\mathbf{u}) \equiv \begin{Bmatrix} 0 \\ \mathbf{q}_c^s(\mathbf{u}^s) \\ \mathbf{q}_d^s(\mathbf{u}^s) \end{Bmatrix}, \tag{31d}$$

$$\mathbf{N} \equiv \begin{Bmatrix} \mathbf{N}_d^f \\ \mathbf{N}_c^f \\ 0 \end{Bmatrix}, \tag{31e}$$

$$\mathbf{g} \equiv \begin{Bmatrix} \mathbf{g}_d^f \\ \mathbf{g}_c^{fs} \\ \mathbf{g}_d^s \end{Bmatrix}, \tag{31f}$$

$$\mathbf{a} \equiv \begin{Bmatrix} \mathbf{a}_d^f \\ \mathbf{a}_c^{fs} \\ \mathbf{a}_d^s \end{Bmatrix}, \tag{31g}$$

$$\mathbf{v} \equiv \begin{Bmatrix} \mathbf{v}_d^f \\ \mathbf{v}_c^{fs} \\ \mathbf{v}_d^s \end{Bmatrix}, \tag{31h}$$

$$\mathbf{u} \equiv \begin{Bmatrix} * \\ \mathbf{u}_c^{fs} \\ \mathbf{u}_d^s \end{Bmatrix}, \tag{31i}$$

8

$$\mathbf{p} \equiv \mathbf{p}^{\mathrm{f}}, \tag{31j}$$

$$_{\mathrm{L}}\mathbf{M}_{cc}^{\mathrm{fs}} \equiv {}_{\mathrm{L}}\mathbf{M}_{cc}^{\mathrm{f}} + {}_{\mathrm{L}}\mathbf{M}_{cc}^{\mathrm{s}}. \tag{31k}$$

where the subscript d indicates the decoupled degrees of freedoms and subscript c indicates the coupled degrees of freedoms.

The time integration of the FSI system is obtained through the predictor-multi-corrector algorithm (PMA) [32, 35] using the Newmark' β method. Let us consider the nonlinear iteration k for the Eqs.(29) and (30) at the current time $t + \Delta t$ as

$$_{\mathrm{L}}\mathbf{M} \, {}^{t+\Delta t}\mathbf{a}^{(k)} + \mathbf{C} \, {}^{t+\Delta t}\mathbf{v}^{(k)} + \mathbf{N} + \mathbf{q}\left({}^{t+\Delta t}\mathbf{u}^{(k)}\right) - \mathbf{G} \, {}^{t+\Delta t}\mathbf{p}^{(k)} = {}^{t+\Delta t}\mathbf{g}, \tag{32a}$$

$$_{\mathrm{T}}\mathbf{G} \, {}^{t+\Delta t}\mathbf{v}^{(k)} = \mathbf{0}. \tag{32b}$$

During the predictor stage of the PMA, the acceleration, velocity, displacement, and pressure at time $t + \Delta t$ are first predicted using those at time t, respectively, as

$$^{t+\Delta t}\mathbf{a}^{(0)} = 0, \tag{33a}$$

$$^{t+\Delta t}\mathbf{v}^{(0)} = {}^{t}\mathbf{v} + \Delta t(1 - \gamma) \, {}^{t}\mathbf{a}, \tag{33b}$$

$$^{t+\Delta t}\mathbf{u}^{(0)} = {}^{t}\mathbf{u} + \Delta t \, {}^{t}\mathbf{v} + \Delta t^2(1/2 - \beta) \, {}^{t}\mathbf{a}, \tag{33c}$$

$$^{t+\Delta t}\mathbf{p}^{(0)} = {}^{t}\mathbf{p}, \tag{33d}$$

where ${}^{t}\mathbf{a}$, ${}^{t}\mathbf{v}$, ${}^{t}\mathbf{u}$, and ${}^{t}\mathbf{p}$ are the known acceleration, velocity, displacement, and pressure, which are obtained from the last time step t, β and γ are the Newmark's parameters that can be chosen so as to obtain numerical stability and integration accuracy, and Δt is the time increment.

The monolithic FSI equation system shown in Eqs.(32a) and (32b) at time $t + \Delta t$ are nonlinear equations. These nonlinear equation system can be linearized using the increments of the accelerations $\Delta\mathbf{a}$, velocity $\Delta\mathbf{v}$, displacement $\Delta\mathbf{u}$, and pressure $\Delta\mathbf{p}$. These increments are obtained from the state variables from the previous nonlinear iteration to the current iteration during the corrector stage of the PMA method defined as [31],

$$^{t+\Delta t}\mathbf{a}^{(k)} = {}^{t+\Delta t}\mathbf{a}^{(k-1)} + \Delta\mathbf{a}, \tag{34a}$$

$$^{t+\Delta t}\mathbf{v}^{(k)} = {}^{t+\Delta t}\mathbf{v}^{(k-1)} + \Delta\mathbf{v} = {}^{t+\Delta t}\mathbf{v}^{(k-1)} + \gamma\Delta t\Delta\mathbf{a}, \tag{34b}$$

$$^{t+\Delta t}\mathbf{u}^{(k)} = {}^{t+\Delta t}\mathbf{u}^{(k-1)} + \Delta\mathbf{u} = {}^{t+\Delta t}\mathbf{u}^{(k-1)} + \beta\Delta t^2\Delta\mathbf{a}, \tag{34c}$$

$$^{t+\Delta t}\mathbf{p}^{(k)} = {}^{t+\Delta t}\mathbf{p}^{(k-1)} + \Delta\mathbf{p}. \tag{34d}$$

Substituting Eqs. (34a)–(34d) into Eq.(32), the following linearized equations in residual form are obtained as

$$\overset{*}{\mathbf{M}}\Delta\mathbf{a} - \mathbf{G}\Delta\mathbf{p} = \Delta\mathbf{g}, \tag{35a}$$

$$\gamma\Delta t \, {}_{\mathrm{T}}\mathbf{G}\Delta\mathbf{a} + \mathbf{G}_{\varepsilon}\Delta\mathbf{p} = \Delta\mathbf{h}, \tag{35b}$$

where $\overset{*}{\mathbf{M}}$ is the generalized mass matrix , $\Delta\mathbf{g}$ and $\Delta\mathbf{h}$ are the residual force vectors, Δ indicates the increment, and $\mathbf{G}_{\varepsilon}$ come from the pressure stabilization term of the pressure-stabilizing/Petrov-Galerkin (PSPG) [34, 36]. The definition of $\overset{*}{\mathbf{M}}$ for the implicit, explicit, and

9

implicit and explicit treatment of the fluid convection term $\mathbf{N}$ and the fluid diffusion term $\mathbf{C}$ can be found in Ref [12, 31]. If the fluid convection and diffusion terms are treated implicitly then

$$\overset{*}{\mathbf{M}} \equiv {}_{\mathrm{L}}\mathbf{M} + \gamma\Delta t(\widetilde{\mathbf{N}} + \mathbf{C}) + \beta\Delta^2\mathbf{K}, \tag{36}$$

where $\widetilde{\mathbf{N}}$ is the Jacobian of the fluid convective vector $\mathbf{N}^{\mathrm{f}}$, and $\mathbf{K}$ is defined using the tangent stiffness matrix of the structure. In case the fluid convection and diffusion terms are treated explicitly then

$$\overset{*}{\mathbf{M}} \equiv {}_{\mathrm{L}}\mathbf{M} + \beta\Delta^2\mathbf{K}. \tag{37}$$

If the fluid convection term is treated explicitly, and the fluid diffusion term is treated implicitly then

$$\overset{*}{\mathbf{M}} \equiv {}_{\mathrm{L}}\mathbf{M} + \gamma\Delta t\mathbf{C} + \beta\Delta^2\mathbf{K}. \tag{38}$$

The FSI monolithic system Eq.(35) is very strongly coupled. However, the monolithic approach is computationally expensive and the monolithic formulations can lead to ill-conditioned equation system [12, 37]. Therefore, in this study, the algebraic splitting also known as projection method proposed by Ishihara and Horie [31] is employed. The algebraic splitting method is computationally efficient and avoids Schur complement without loss of robustness. This method has been successfully used for fluid-structure interaction analysis in the flapping flexible wing [2, 38] and hierarchal decomposition of the structure-fluid-electrostatic interaction in a MEMS micro cantilever [25]. The projection method is summarized as follows:

From the fluid-structure interaction equilibrium Eq.(32a), the state variables are predicted as the intermediate state variables for the known fluid pressure ${}^{t+\Delta t}\mathbf{p}^{(k-1)}$. Then, Eq.(32a) is linearized as

$$\overset{*}{\mathbf{M}}\Delta\hat{\mathbf{a}} = \Delta\mathbf{g}, \tag{39}$$

where the intermediate state variables and their increments are described as

$$ {}^{t+\Delta t}\hat{\mathbf{a}}^{(k)} = {}^{t+\Delta t}\mathbf{a}^{(k-1)} + \Delta\hat{\mathbf{a}}, \tag{40a}$$

$$ {}^{t+\Delta t}\hat{\mathbf{v}}^{(k)} = {}^{t+\Delta t}\mathbf{v}^{(k-1)} + \Delta\hat{\mathbf{v}} = {}^{t+\Delta t}\mathbf{v}^{(k-1)} + \gamma\Delta t\Delta\hat{\mathbf{a}}, \tag{40b}$$

$$ {}^{t+\Delta t}\hat{\mathbf{u}}^{(k)} = {}^{t+\Delta t}\mathbf{u}^{(k-1)} + \Delta\hat{\mathbf{u}} = {}^{t+\Delta t}\mathbf{u}^{(k-1)} + \beta\Delta t^2\Delta\hat{\mathbf{a}}, \tag{40c}$$

where ${}^{t+\Delta t}\hat{\mathbf{a}}^{(k)}$, ${}^{t+\Delta t}\hat{\mathbf{v}}^{(k)}$, and ${}^{t+\Delta t}\hat{\mathbf{u}}^{(k)}$ are the intermediate or predicted acceleration, velocity and displacement, respectively. Subtracting both sides of Eq.(39) from Eq.(35a), after suitable arrangement,

$$\gamma\Delta t\mathbf{G}\Delta\mathbf{p} = \overset{*}{\mathbf{M}}\left({}^{t+\Delta t}\mathbf{v}^{(k)} - {}^{t+\Delta t}\hat{\mathbf{v}}^{(k)}\right). \tag{41}$$

By left multiplying both sides of Eq.(41) with ${}_{\mathrm{T}}\mathbf{G}_{\mathrm{L}}\mathbf{M}^{-1}$ to obtain,

$$\begin{aligned}
\gamma\Delta t \,{}_{\mathrm{T}}\mathbf{G}_{\mathrm{L}}\mathbf{M}^{-1}\mathbf{G}\Delta\mathbf{p} = {}_{\mathrm{T}}\mathbf{G}^{t+\Delta t}\mathbf{v}^{(k)} - {}_{\mathrm{T}}\mathbf{G}^{t+\Delta t}\hat{\mathbf{v}}^{(k)} \\
+ {}_{\mathrm{T}}\mathbf{G}_{\mathrm{L}}\mathbf{M}^{-1}\overline{\mathbf{M}}^{*}\left({}^{t+\Delta t}\mathbf{v}^{(k)} - {}^{t+\Delta t}\hat{\mathbf{v}}^{(k)}\right),
\end{aligned} \tag{42}$$

where $\overline{\mathbf{M}}^* = \overset{*}{\mathbf{M}} - {}_{\mathrm{L}}\mathbf{M}$. If the following pressure Poisson equation (PPE),

$$\gamma \Delta t \; {}_{\mathrm{T}}\mathbf{G}_{\mathrm{L}}\mathbf{M}^{-1}\mathbf{G}\Delta\mathbf{p} = -{}_{\mathrm{T}}\mathbf{G}^{t+\Delta t}\hat{\mathbf{v}}^{(k)}, \tag{43}$$

is solved, then Eq.(42) is reduced as

$$ {}_{\mathrm{T}}\mathbf{G}^{t+\Delta t}\mathbf{v}^{(k)} + {}_{\mathrm{T}}\mathbf{G}_{\mathrm{L}}\mathbf{M}^{-1}\overline{\mathbf{M}}^* \left({}^{t+\Delta t}\mathbf{v}^{(k)} - {}^{t+\Delta t}\hat{\mathbf{v}}^{(k)} \right) = \mathbf{0}. \tag{44}$$

When the nonlinear iterations are convergent, the predicted velocity ${}^{t+\Delta t}\hat{\mathbf{v}}^{(k)}$ agrees with ${}^{t+\Delta t}\mathbf{v}^{(k)}$ asymptotically as

$$ |\; {}^{t+\Delta t}\mathbf{v}^{(k)} - {}^{t+\Delta t}\hat{\mathbf{v}}^{(k)} \;| \to 0 \qquad \text{as} \qquad k \to \mathbf{0} \tag{45}$$

The second term of the Eq.(44) will vanish asymptotically in the nonlinear iterations, and the incompressibility constraint for the current fluid velocity ${}^{t+\Delta t}\mathbf{v}^{(k)}$ is satisfied as

$$ {}_{\mathrm{T}}\mathbf{G}^{t+\Delta t}\mathbf{v}^{(k-1)} = \mathbf{0}. \tag{46}$$

In summary, Eq.(39) is solved to determine the increment of the intermediate acceleration $\Delta\hat{\mathbf{a}}$ for the previous pressure. Once $\Delta\hat{\mathbf{a}}$ is evaluated, then the intermediate velocity ${}^{t+\Delta t}\hat{\mathbf{v}}^{(k)}$ is solved using Eq.(40b). After that, the pressure increment $\Delta\mathbf{p}$ is obtained solving Eq.(43). Next the acceleration increment $\Delta\mathbf{a}$ is solved using Eq.(35a), and Eq.(34a), Eq.(34b), and Eq.(34c) are solved to derive the acceleration ${}^{t+\Delta t}\mathbf{a}^{(k)}$, the velocity ${}^{t+\Delta t}\mathbf{v}^{(k)}$, and the displacement ${}^{t+\Delta t}\mathbf{u}^{(k)}$, respectively.

3.3. Hierarchically Decomposed Piezoelectric-Structure-Fluid Interaction

The strongly coupled piezoelectric-structure-fluid interaction is hierarchically decomposed, which is shown in Fig. 2, as follows: At the first level, the triply coupled system is partitioned into subsystems of piezoelectric field and fluid-structure interaction (FSI). These two fields are coupled using the block the Gauss-Seidel iterative method. In the second level, the FSI subsystem is further decomposed using the projection method, i.e., the FSI is split into the fluid-structure velocity field and the pressure field using algebraic splitting. In the third level, the structure-fluid velocity field is further partitioned into the structure velocity field and the fluid velocity field using the explicit time integration for the fluid interior DOFs. This decomposition allows us to employ 3D solid element to solve piezoelectric field, shell element to solve inverse-piezoelectric effect, and P1P1 element to solve the fluid field, which remedies the shortcoming of using a single finite element mesh for all three fields.

The piezoelectric system in 3D solid elements is given by

$$ {}^{t+\Delta t}\mathbf{K}_{\phi\phi}^{(i)}\; {}^{t+\Delta t}\phi_{\mathrm{solid}}^{(i)} = {}^{t+\Delta t}\mathbf{q} - {}^{t+\Delta t}\mathbf{K}_{\phi u}^{(i)}\; {}^{t+\Delta t}\mathbf{u}_{\mathrm{solid}}^{(i-1)}. \tag{47}$$

Using the displacement transformation Eq.(23) from the shell element to the 3D solid element, the above equation becomes

$$ {}^{t+\Delta t}\mathbf{K}_{\phi\phi}^{(i)}\; {}^{t+\Delta t}\phi_{\mathrm{solid}}^{(i)} = {}^{t+\Delta t}\mathbf{q} - {}^{t+\Delta t}\mathbf{K}_{\phi u}^{(i)}\; {}_{\mathrm{u}}\mathbf{T}\; {}^{t+\Delta t}\mathbf{u}^{s(i-1)}. \tag{48}$$

where superscript i indicates the current BGS iteration. The electric potential ${}^{t+\Delta t}\phi_{\mathrm{solid}}^{(i)}$ of current iteration i is evaluated in the 3D solid elements using the displacements of the shell
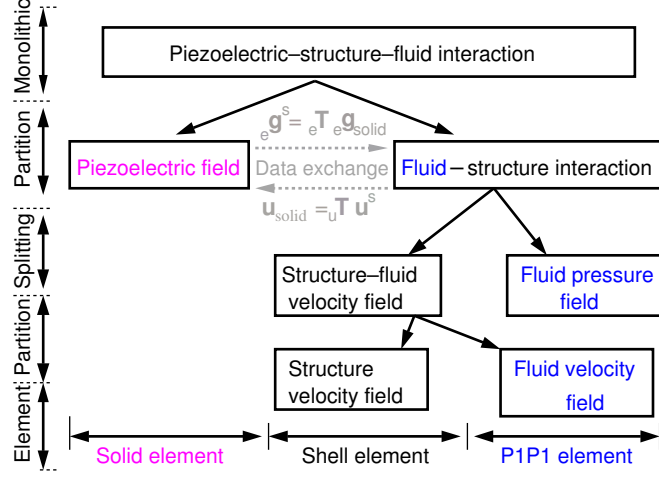
Fig. 2. Hierarchal decomposition for the piezoelectric-structure-fluid interaction system

elements obtained in the previous iteration $i - 1$. We obtain the electrical forces $_e\mathbf{g}$ for the known electric potential in the current BGS iteration i at each time step $t + \Delta t$ in the 3D solid elements as

$$^{t+\Delta t}_e\mathbf{g}_{\text{solid}} = -\,^{t+\Delta t}\mathbf{K}^{(i)}_{u\phi}\,^{t+\Delta t}\phi^{(i)}_{\text{solid}}. \tag{49}$$

The induced electrical force vector is now applied on to the shell structure of the FSI system through the force transformation relation given in Eq.(20), which gives us $_e\mathbf{g}^s$. After the force transformation, the external force vector $\mathbf{g}$ given in Eq.(31f) becomes

$$\mathbf{g} \equiv \begin{Bmatrix} \mathbf{g}^f_d \\ \mathbf{g}^{fs}_c \\ \mathbf{g}^s_d \end{Bmatrix} \Longrightarrow \mathbf{g} \equiv \begin{Bmatrix} \mathbf{g}^f_d \\ \mathbf{g}^{fs}_c + _e\mathbf{g}^s_c \\ \mathbf{g}^s_d + _e\mathbf{g}^s_d \end{Bmatrix}, \tag{50}$$

where $_e\mathbf{g}^s = [_e\mathbf{g}^s_c,\ _e\mathbf{g}^s_d]^{\mathrm{T}}$, and $_e\mathbf{g}^s_c$ is the external force or transnational force acting on the shell and $_e\mathbf{g}^s_d$ is the external electric moment of force or rotational force acting on the shell, as shown in Fig. 3. The transnational force acting on the shell are obtained using [15]

$$_e\mathbf{g}^s_c = \sum_{n_r=1}^{N_r} {}_e\mathbf{g}^{n_r}_{\text{solid}} + \sum_{n_s=1}^{N_s} \frac{_e\mathbf{g}^{n_s}_{\text{solid}}}{2}, \tag{51}$$

where $n_r = 1, \ldots, N_r$ are the indices of the solid element nodes that are located along the considered director vectors $\mathbf{V}^k_n$ of the shell nodes as shown in Fig. 3, and $_e\mathbf{g}^{n_r}_{\text{solid}}$ is the induced nodal electric force vector at solid node n_r. Similarly, $n_s = 1, \ldots, N_s$ are the indices of the solid element nodes that are located not along the considered director vector of the shell nodes but directly adjacent to it, and $_e\mathbf{g}^{n_s}_{\text{solid}}$ is the induced nodal electric force vector at solid node n_s. The rotational force acting on the shell $_e\mathbf{g}^s_d$ are obtained using

$$_e\mathbf{g}^s_d = \sum_{n_r=1}^{N_r} (\mathbf{d}^{n_r} \times {}_e\mathbf{g}^{n_r}_{\text{solid}}) + \sum_{n_s=1}^{N_s} (\mathbf{d}^{n_s} \times \frac{_e\mathbf{g}^{n_s}_{\text{solid}}}{2}), \tag{52}$$

12

where $\mathbf{d}^{n_r}$ and $\mathbf{d}^{n_s}$ are the position vectors of the solid element nodes n_r and n_s, respectively, with respect to the shell mid-surface nodes. After the force transformation onto the shell structure, the fluid-structure interaction is analyzed using the projection method at current BGS iteration i as follows:

The increment of intermediate acceleration at the current BGS and nonlinear iteration is determined for the known pressure $^{t+\Delta t}\mathbf{p}^{(i)(k-1)}$ by solving

$$\overset{*}{\mathbf{M}}\Delta\hat{\mathbf{a}}^{(i)} = \Delta\mathbf{g}^{(i)}. \tag{53}$$

Using $\Delta\hat{\mathbf{a}}^{(i)}$, the intermediate state variables and their increment given in Eq.(40) are evaluated at each BGS and nonlinear iteration as

$$^{t+\Delta t}\hat{\mathbf{a}}^{(i)(k)} = {}^{t+\Delta t}\mathbf{a}^{(i)(k-1)} + \Delta\hat{\mathbf{a}}^{(i)}, \tag{54a}$$

$$^{t+\Delta t}\hat{\mathbf{v}}^{(i)(k)} = {}^{t+\Delta t}\mathbf{v}^{(i)(k-1)} + \Delta\hat{\mathbf{v}}^{(i)} = {}^{t+\Delta t}\mathbf{v}^{(i)(k-1)} + \gamma\Delta t\Delta\hat{\mathbf{a}}^{(i)}, \tag{54b}$$

$$^{t+\Delta t}\hat{\mathbf{u}}^{(i)(k)} = {}^{t+\Delta t}\mathbf{u}^{(i)(k-1)} + \Delta\hat{\mathbf{u}}^{(i)} = {}^{t+\Delta t}\mathbf{u}^{(i)(k-1)} + \beta\Delta t^2\Delta\hat{\mathbf{a}}^{(i)}, \tag{54c}$$

The pressure increment at the current BGS and nonlinear iterations is obtained using the intermediate velocity by solving

$$\gamma\Delta t \, {}_{\mathrm{T}}\mathbf{G}_{\mathrm{L}}\mathbf{M}^{-1}\mathbf{G}\Delta\mathbf{p}^{(i)} = -{}_{\mathrm{T}}\mathbf{G}^{t+\Delta t}\hat{\mathbf{v}}^{(i)(k)}. \tag{55}$$

Then the acceleration increment is solved using

$$\overset{*}{\mathbf{M}}\Delta\mathbf{a}^{(i)} - \mathbf{G}\Delta\mathbf{p}^{(i)} = \Delta\mathbf{g}^{(i)}. \tag{56}$$

Now the correct phase of the PMA given in Eq.(34) is executed to solve for the acceleration $^{t+\Delta t}\mathbf{a}^{(i)(k)}$, the velocity $^{t+\Delta t}\mathbf{v}^{(i)(k)}$, and the displacement $^{t+\Delta t}\mathbf{u}^{(i)(k)}$ at current BGS and nonlinear iterations of every time step. At the correct stage, we obtain the structural displacements in the shell solving the geometric nonlinear structure equilibrium equation which is used to solve the piezoelectric field in the 3D solid given as

$$^{t+\Delta t}\mathbf{u}^{\mathrm{s}(i)(k)} = {}^{t+\Delta t}\mathbf{u}^{\mathrm{s}(i)(k-1)} + \Delta\mathbf{u}^{\mathrm{s}(i)}. \tag{57}$$

In an incremental formulation based on the Newton-Raphson iteration method, the increment in the internal energy is used to terminate the N–R iteration loop [39]. The resultant displacements in the shell element is now transformed to the solid element using displacement transformation at every BGS iteration to analyze the piezoelectric field. Eq.(23) is rewritten as

$$^{t+\Delta t}\mathbf{u}^{(i)}_{\mathrm{solid}} = {}_{\mathrm{u}}\mathbf{T} \, {}^{t+\Delta t}\mathbf{u}^{\mathrm{s}(i)}. \tag{58}$$

The components of the transformation matrix $_{\mathrm{u}}\mathbf{T}$ are obtained from the displacement interpolation function at time t as in the shell element [40] using

$$^{t}\mathbf{u}^{\mathrm{s}}_{j} = h^{n}(r_1, r_2) \, {}^{t}_{n}\mathbf{u}^{\mathrm{s}}_{j} + \frac{r_3}{2}a \, h^{n}(r_1, r_2)(-\alpha^{n}\mathbf{V}^{n}_{2} + \beta^{n}\mathbf{V}^{n}_{1}), \tag{59}$$

where $^{t}\mathbf{u}^{\mathrm{s}}_{j}$ are the displacements of a material point in a shell element at time t with natural coordinates (r_j), n represents shell node, $^{t}_{n}\mathbf{u}^{\mathrm{s}}_{j}$ is the displacement vector of the shell node n at time t, h^{n} are the element shape function, a is the shell thickness, and α^{n} and β^{n} are rotations about

13

$\mathbf{V}_1^n$ and $\mathbf{V}_2^n$, respectively. The coupling strategy of the triply coupled piezoelectric-structure-fluid system is symbolically represented using the model equation system including the degrees of freedoms (DOFs) of fluid, structure and piezoelectric fields as shown in Fig. 4.
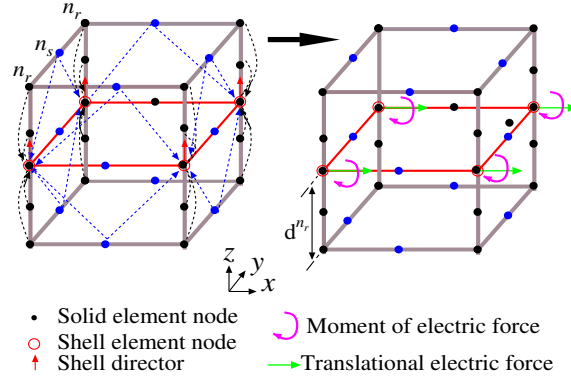

Fig. 3. Electric force and moment of electric force transformation

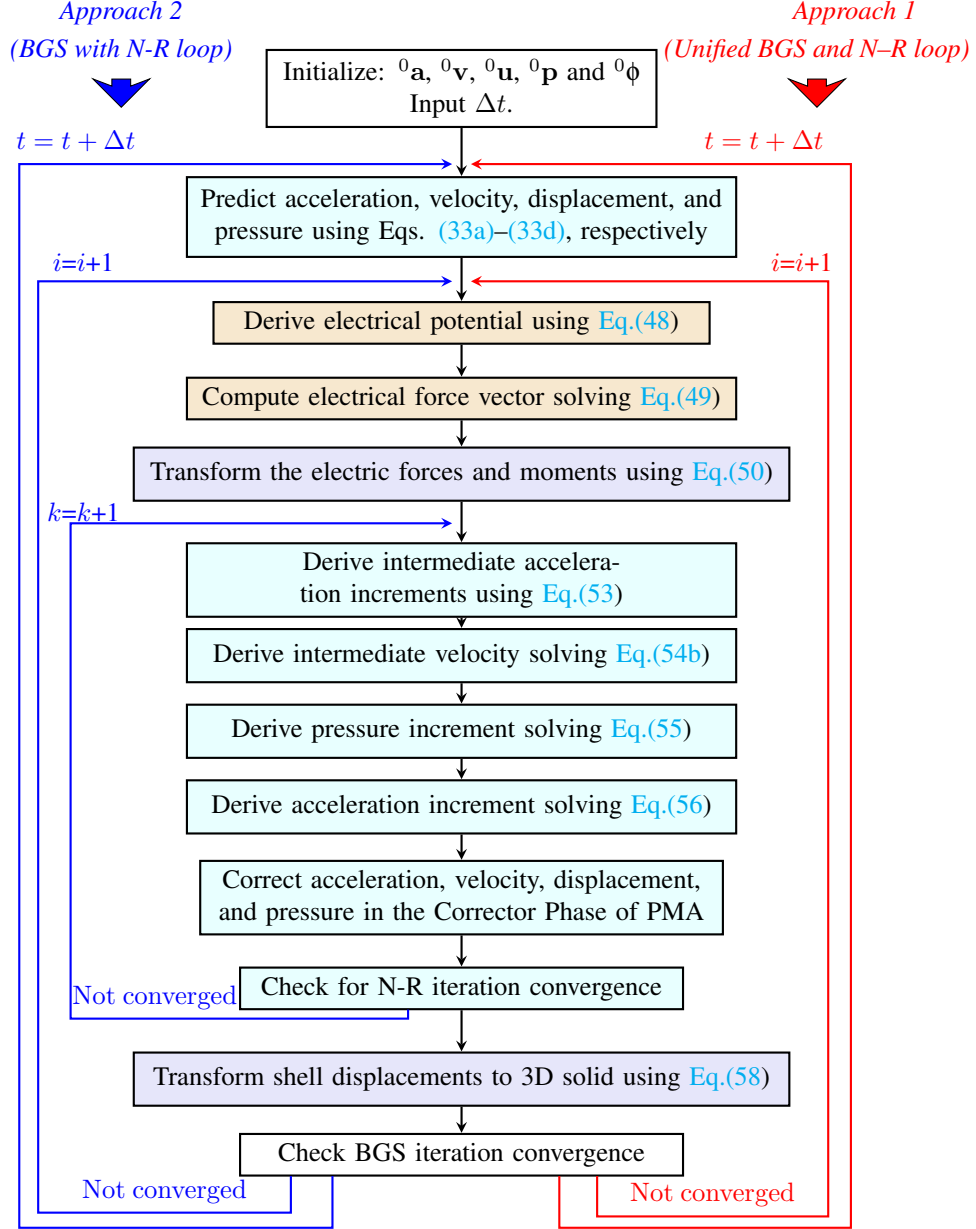**Fig. 4.** Piezoelectric-structure-fluid coupling: Data flow between piezoelectric and FSI systems.

14

Approach 2
(BGS with N-R loop)

Approach 1
(Unified BGS and N–R loop)

Initialize: $^0\mathbf{a}$, $^0\mathbf{v}$, $^0\mathbf{u}$, $^0\mathbf{p}$ and $^0\phi$
Input Δt.

$t = t + \Delta t$

$t = t + \Delta t$

Predict acceleration, velocity, displacement, and pressure using Eqs. (33a)–(33d), respectively

$i=i+1$

$i=i+1$

Derive electrical potential using Eq.(48)

Compute electrical force vector solving Eq.(49)

Transform the electric forces and moments using Eq.(50)

$k=k+1$

Derive intermediate acceleration increments using Eq.(53)

Derive intermediate velocity solving Eq.(54b)

Derive pressure increment solving Eq.(55)

Derive acceleration increment solving Eq.(56)

Correct acceleration, velocity, displacement, and pressure in the Corrector Phase of PMA

Check for N-R iteration convergence

Not converged

Transform shell displacements to 3D solid using Eq.(58)

Check BGS iteration convergence

Not converged

Not converged

Fig. 5. Solution procedure of the proposed piezoelecctric-structure-fluid interaction
▢ Piezoelectric solver, ▢ FSI solver, ▢ force and displacement transformation.

Fig. 5 shows the analysis procedure to solve piezoelectric-structure-fluid interaction. The BGS iteration loop is used to couple the variables between the piezoelectric field and the FSI system. This loop is repeated until the desired tolerance is satisfied. When the problem is geometrically nonlinear, a second inner loop (Newton-Raphson iterations) is performed for the

structural part. Again, this N-R loop is repeated until the increment in the internal energy criteria is satisfied. To manage the BGS and N-R iteration loops in piezoelectric-structure-fluid interaction, we propose two approaches similar to that of piezoelectric-structure interaction in Ref.[15]. The purpose of studying these approaches is to check the computational efficiency, convergence property, and accuracy.

1. *Approach 1: Unified BGS and N-R loops*

   In this approach, the BGS and N-R loops are unified into a single loop, therefore, we call this approach as unified BGS and N-R loops. Here, we use the term nonlinear iterations to indicate the unified iteration BGS and N-R iterations. The analysis flow of this approach is illustrated in the right side of Fig. 5 with the red color lines and labels, where i indicates the nonlinear iteration loop or unified BGS and N-R iteration loop. For this approach, Eq.(57) is modified as

   $$^{t+\Delta t}\mathbf{u}^{s(i)} = {}^{t+\Delta t}\mathbf{u}^{s(i-1)} + \Delta\mathbf{u}^{s(i)}. \tag{60}$$

2. *Approach 2: BGS iteration with the N-R loop*

   In this approach, for every BGS iteration, several N-R iterations are evaluated until the increment in the internal energy of the structure is lesser than the prescribed energy tolerance value [39]. The BGS iteration loop is terminated based on the structure relative displacement error between the current and previous iterations [13]. We call this approach as BGS iteration with the N-R loop. The analysis flow of this approach is illustrated on the left side of Fig. 5 with the blue color lines and labels.

4. Numerical Example: Analysis of thin piezoelectric bimorph in converging fluid channel

A flexible restrictor flap in the converging channel is one of the FSI benchmark problems, which was proposed by Mok and Wall [33] in order to demonstrate the computational efficiencies, convergence properties, stability performances, mesh sensitivities, and the coupling between fluid and structure using partitioned finite element algorithm. Several authors in Refs. [31, 33, 41–44] have studied this numerical example to validate their FSI algorithm. Ishihara and Horie in Ref.[31] had analyzed the same problem to discuss the convergence properties, computational efficiency, and stability performances of the projection method. Their results are close to the solutions from the literature (Mok et al. [33] and Neumann et al. [41]). In the above mentioned studies, the flexible structure is shown in Fig. 6 is made of a rubber material with the material density $\rho^s = 1500$ kg/m^3, Young's modulus $E^s = 2.3$MPa, and a Poisson's ratio $v^s = 0.45$. The fluid is silicone oil. The mass density and the viscosity of silicone oil used in the analysis are $\rho^f = 956$ kg/m^3 and $\mu^f = 0.145$kg/(m.s). The inflow velocity of the fluid has a parabolic shape. The fluid velocity at the top v_{in} varies as $\frac{V_{max}}{2}(1 - \cos\frac{\pi t}{10})$ until 10 sec and V_{max} after 10 sec. The value of V_{max} is 0.06067 m/s and $f = 0.05$Hz.

4.1. Numerical setup

In the present study, a piezoelectric bimorph is used instead of a rubber. Two separate piezoelectric materials are studies. One is Polyvinylidene fluoride (PVDF), and the other one is lead zirconate titanate (PZT). The mechanical and electric properties of these piezoelectric materials that are used in the analysis are given in Table 1. As shown in Table 1, the piezoelectric stress constants, piezoelectric strain constants, and electromechanical coupling factor of PZT-5H
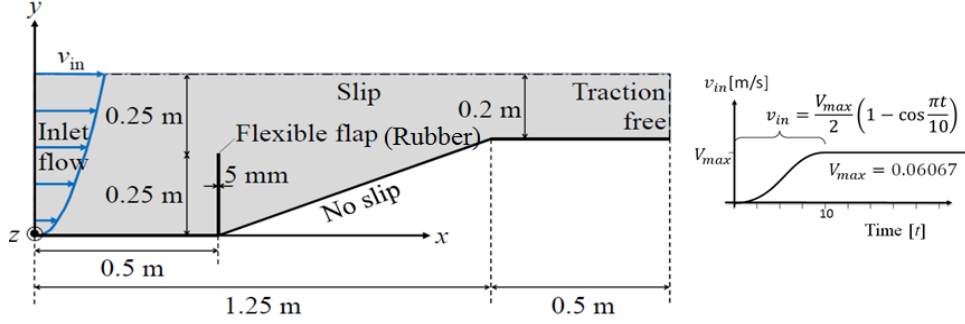
Fig. 6. A flexible restrictor flap in converging fluid channel

material is very high compared to that of PVDF. The reason why these two piezoelectric materials are used is that they have different mechanical, electrical and electromechanical properties. The piezoelectric ceramic PZT-5H has a very strong direct and inverse piezoelectric coupling effect than that of the piezoelectric polymer PVDF. Four test cases involving different loading conditions and electric configurations are investigated.

1. In case 1, the *actuator setup* is used for the piezoelectric bimorph configuration with a series connection wherein a uniform potential is applied onto the top surface of the bimorph while the bottom surface being earthed as shown in Fig. 7(a) and the piezoelectric layers are polarized opposite to each other in the thickness direction. The bimorph is subjected to an applied AC voltage $V_\phi = V_{\phi_0} \sin\omega_\phi t$.

2. In case 2, *pure FSI* analysis is performed for the structural properties of a PVDF and PZT-5H with the sinusoidal external mechanical force, which is equivalent to the induced electric force in the actuator problem also known as blocking force [45] is applied to the tip of the flap as shown in Fig. 7(b). The blocking force for the applied electric field E_3 can be obtained as [45],

$$F_{\text{ext0}} = \frac{3wt^2 E^{\text{s}}}{8L} d_{31} E_3, \tag{61}$$

where w is the width of the piezoelectric bimorph, $t = 2t_p$ is the thickness of the bimorph, t_p is the thickness of each piezoelectric layer, E^{s} is the Young's modulus of the piezoelectric bimorph, L is the length of the bimorph, and d_{31} is the piezoelectric strain constant. If the piezoelectric layers are connected in series, then the applied electric field in the thickness direction across the piezoelectric layers is $E_3 = V_{\phi0}/2t_p$. In this problem setup, the piezoelectric field is not considered, instead only pure FSI analysis with external mechanical forces at the tip of the shell structure along with the fluid boundary condition is imposed. This blocking force is applied sinusoidally as $F_{\text{ext}} = F_{\text{ext0}} \sin\omega t$. The amplitude of the external force F_{ext0} corresponding to $V_{\phi0} = 100$ V for PVDF and PZT-5H bimorph configurations with series connection calculated using the relation given in Eq.(61) are 6.90×10^{-4} N and 0.0786N, respectively.

3. In case 3, *closed or short circuit sensor setup* is used for a piezoelectric bimorph where the top and bottom surfaces of the bimorph are set to zero electric potential and a transverse

17

mechanical force which is equivalent to the induced electric force in the actuator setup is applied to the free end of the shell structure made of the piezoelectric material as shown in Fig. 7(c). The piezoelectric layers are polarized in opposite to each other in the thickness direction. The external force used here is the same as that used in case 2, and it is known as the blocking force [45].

4. In case 4, *open circuit sensor setup* is used for a piezoelectric bimorph where the top and bottom surfaces of the bimorph are in an open circuit condition and a transverse mechanical force which is equivalent to the induced electric force in the actuator setup is applied to the free end of the shell structure made of the piezoelectric material as shown in Fig. 7(d). The piezoelectric layers are polarized in opposite to each other in the thickness direction. The external force used here is the same as that used in case 2 and case 3.

For all these cases, the inlet fluid velocity boundary condition in the converging channel follows the setup shown in Fig. 6. The fluid domain of the channel is modeled using P1P1 elements [34] (12,012 nodes and 33,600 elements) shown in Fig. 8(a), the structural mesh of the piezoelectric cantilever beam is modeled using shell elements [46] (42 nodes and 20 elements) shown in Fig. 8(b), and the electrical field is modeled using 3D solid elements (20 node hexahedron element) shown in Fig. 8(c) consists of 683 nodes and 80 elements. Both the fluid and structural meshes have single division along the z-direction as shown in Fig. 8(a) and (b), while the electrical mesh has 4 divisions along x-direction as shown in Fig. 8(c). Note that the z dimension of the fluid domain also has 0.02m and the boundary conditions are imposed such that the phenomena are restricted in the xy planes.
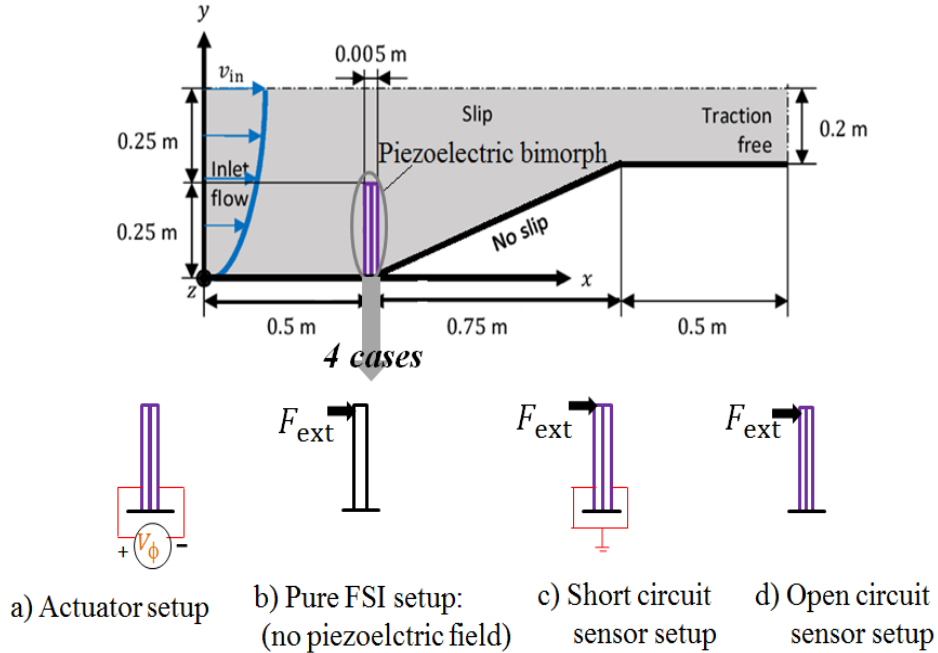

Fig. 7. Thin piezoelectric bimorph in converging fluid channel
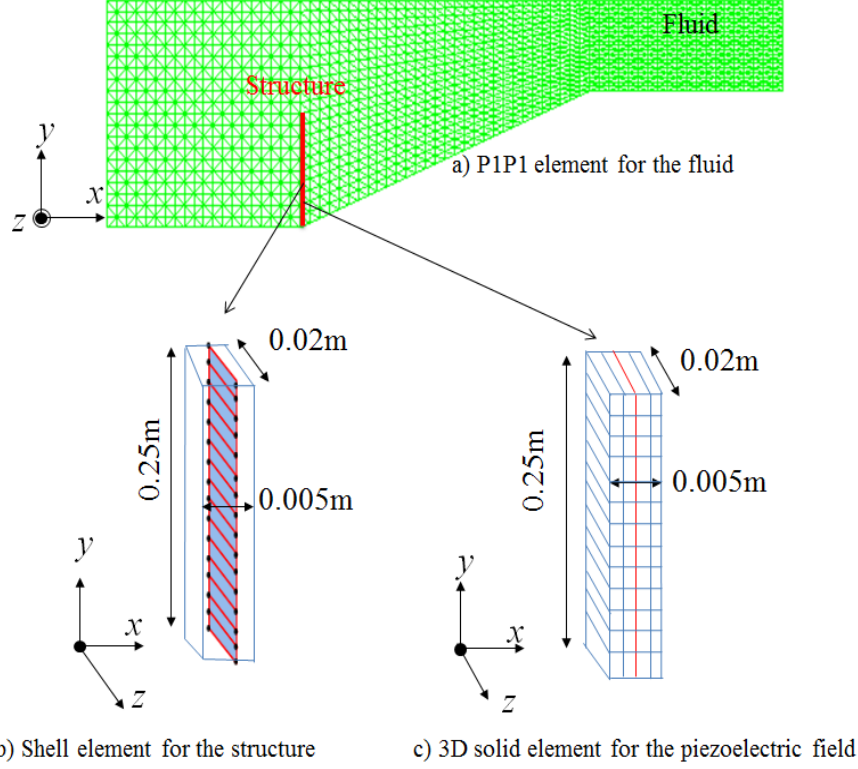
18

Fig. 8. The finite element meshes: a) P1P1 elements for the fluid, b) shell for the thin structure, c) 3D solid elements for the piezoelectric field (the graphics is enlarged in thickness x-direction for better visibility)

4.2. Results and discussions

4.2.1. Resonance frequency of piezoelectric bimorph: Theory

The theoretical solution for the resonance frequency of the bimorph cantilever beam immersed in the fluids is given as [47]

$$
\omega_{\text{fld}}^{(n)} = \omega_{\text{vac}}^{(n)} \left[1 + \frac{\pi \rho^{\text{f}} \text{w}}{4 \rho^{\text{s}} h} \Gamma^{\text{f}}(m) \right]^{-1/2}, \tag{62}
$$

where ρ^{f} and ρ^{s} are the density of the fluid and the structure, respectively, w and h are the width and the thickness of the structure, m is the normalized mode numbers, $\Gamma^{\text{f}}(m)$ is the hydrodynamic function and $\omega_{\text{vac}}^{(n)}$ is the nth resonant frequency in a vacuum. In general, the 1st bending resonance frequency of the cantilever beam operating transversely in viscous liquid media is found to shift to a lower value compared to that in the vacuum or air [48].

Table 1: Material properties of PVDF and PZT-5H used in the numerical analysis of a piezoelectric bimorph in converging fluid channel (the absolute permitivity $\varepsilon_0 = 8.854$ pF/m)

	PVDF[8]	PZT-5H [49]
Young's Modulus (GPa)		
E_{11}	2.0	62.0
E_{33}	2.0	50.0
Elastic stiffness (GPa)		
C_{11}	2.62	115.0
C_{12}	1.07	68.5
C_{13}	1.07	68.9
C_{33}	2.62	101.5
C_{44}	0.775	20.3
C_{66}	0.775	23.3
Density (kg/m^3)		
ρ_p	1800	7360
Poission's ratio		
v_p	0.29	0.30
Piezoelectric stress constants (C/m^2)		
e_{31}	0.046	-5.01
e_{33}	-	24.0
e_{15}	-	14.7
Piezoelectric strain constants (pC/N)		
d_{31}	23.0	-262
d_{33}	-	518
d_{15}	-	726
Absolute permitivity ($\times 10^{-10}$ F/m)		
ε_{11}	1.06	245.9
ε_{33}	1.06	280.6
Electromechanical coupling factor		
k_{31}	0.12	-0.386
k_{33}	-	0.683
k_{15}	-	0.660

4.2.2. Numerical result

At first, we present the iteration convergence properties of both the approaches for the numerical setup given in Fig. 7(a) for a bias voltage $V_{\phi0} = 100$V at a frequency $\omega_\phi = 50.0$ rad/s with the fluid boundary condition which is shown in Fig. 6 and a time increment $\Delta t = 5.0 \times 10^{-3}$s. Fig. 9(a) shows the increment in the internal energy which is obtained by multiplying the residual force vector and the incremental displacement vector and Fig. 9(b) shows the relative error in the tip deflection at every nonlinear iteration i with the unified approach. To plot these graphs, the number of nonlinear iterations is fixed to 10. As shown in Fig. 9(a), when the nonlinear iteration reaches 4, the increment in the internal energy satisfies the preassigned energy tolerance value $e_{\text{tol}} = 1.0 \times 10^{-12}$. However, to achieve displacement convergence condition at least 6 nonlinear iterations are needed, as shown in Fig. 9(b). Notice that, in Fig. 9(b), for the first few time steps until $t = 1$s, many nonlinear iterations are needed satisfying displacement convergence criteria. The nonlinear iteration loop automatically exits when the displacement convergence criteria is

satisfied.
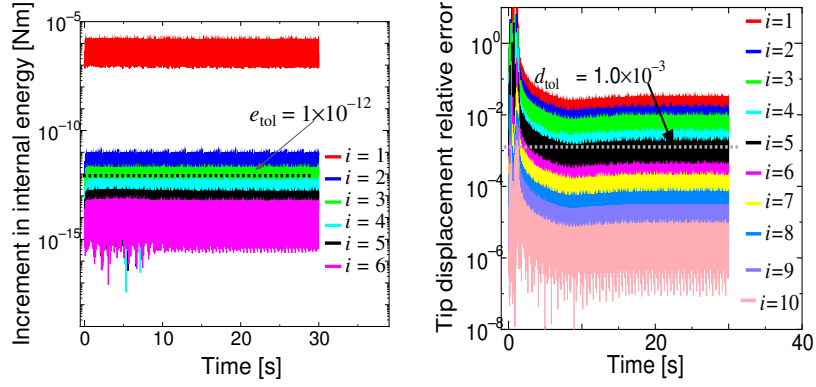
(a) Increment in the internal energy vs nonlinear iterations

(b) Deflection relative error vs nonlinear iterations

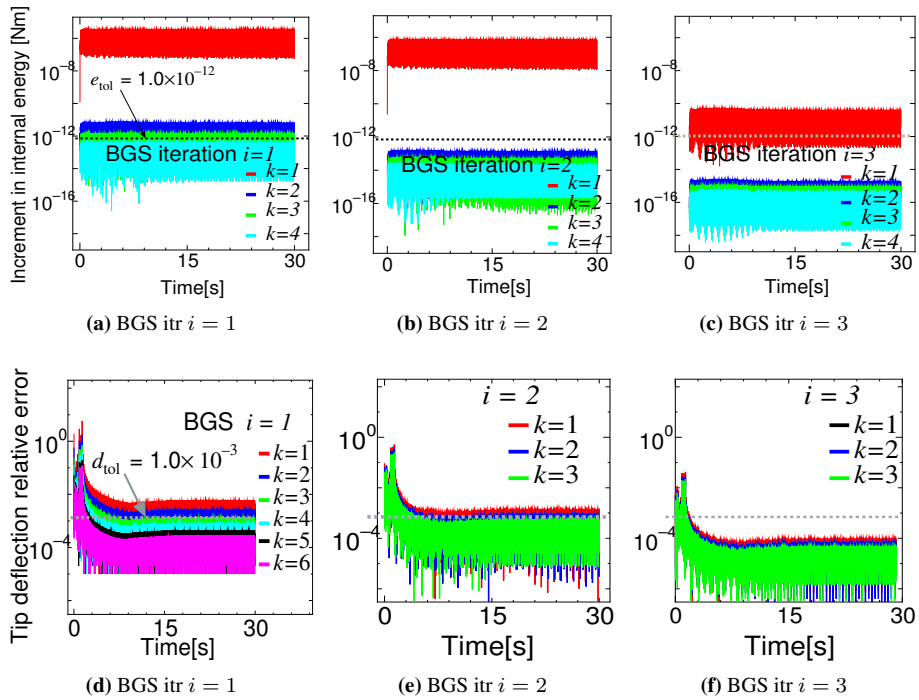**Fig. 9.** Iteration convergence properties of Approach 1: unified BGS and N-R loops

(a) BGS itr $i = 1$

(b) BGS itr $i = 2$

(c) BGS itr $i = 3$

(d) BGS itr $i = 1$

(e) BGS itr $i = 2$

(f) BGS itr $i = 3$

Fig. 10. Iteration convergence properties of Approach 2: BGS iteration with N-R loop

Fig. 10 shows the iteration convergence properties of the second approach, i.e., the BGS iteration with the N-R loop. Here, Figs. 10(a)–10(c) show the time histories of the increment in

21

the internal energy at every BGS iteration i and N-R iteration k. To plot these graphs, the number of N-R iteration is fixed to 6 while the BGS iteration is fixed to 6. For the sake of convenience, the convergence properties of only first three BGS iterations are shown in Figs. 10(a)–10(c). At the first BGS iteration, four N-R iterations are required to satisfy the preassigned energy tolerance of e_{tol} while the second BGS iteration requires three N-R iterations, and the subsequent BGS iterations requires two N-R iterations to satisfy the tolerance condition. At each BGS iteration, the N-R iteration convergence condition is satisfied. Figs. 10(d)–10(f) shows the time histories of the tip displacement relative error in each N-R iteration of every BGS iteration. This conventional approach takes many numbers of N-R iterations than unified BGS and N-R loops approach to achieve energy tolerance and relative error in displacement at every time step.

Now, the comparison of the actual computational time of the two approaches is demonstrated. We use the parallel computation based on the domain decomposition method [50], where the fluid domain is decomposed into the six subdomains considering the computational load balancing. The structure and piezoelectric domains are solved together with one of the fluid subdomains. We use a multi-core processor, where the clock frequency of each core is 2.2GHz. Table 2 shows the actual computing time to solve one time step with the nonlinear iterations $i = 1$, 2, ..., 6 in the unified approach, where the FSI and piezoelectric analyses consume about 74% and 26% of the time respectively. From the iteration convergence results of the unified algorithm shown in Fig. 9, at least 6 nonlinear iterations are desired to obtain a converged solution. Therefore, the desired computing time to solve one time step with the unified approach is 2379 ms. Table 3 shows the computing time to solve one time step with the BGS iteration with the N-R loop approach. Based on the convergence results of the BGS iteration with the N-R loop approach shown in Fig. 10, 5 BGS iterations consisting of a total of 11 N-R iterations are required. Therefore, the desired computing time to solve one time step with the BGS iteration with the N-R loop approach is 4348 ms as shown in Table 3. Therefore, the unified approach is computationally efficient than the BGS iteration with the N-R loop. Hence, in the following sections, the unified approach is used.

Table 2: Actual computing time to solve one time step with the nonlinear iterations in the unified approach or Approach 1

Nonlinear iteration	Computational time [ms]
1	397
2	397
3	397
4	395
5	396
6	397

22

Table 3: Actual computing time to solve one time step with the BGS and N-R iterations in Approach 2

BGS iteration	N-R iteration	Computing time [ms]
1	1	395
	2	395
	3	395
	4	395
2	1	395
	2	395
	3	395
3	1	396
	2	395
4	1	396
5	1	396

Next, the influence of time increment on the number of nonlinear iteration is shown for the unified approach. The critical time increment is given approximately 0.4 sec from the Courant number condition, as discussed in the previous FSI analysis for the channel with a flexible flap made of rubber [31]. Fig. 11 shows the relationship between the time increment Δt and the number of nonlinear iterations to obtain a converged solution at the time $t = 10$ sec for the actuator setup with the applied voltage $V_{\phi_0} = 100V$ at a frequency $\omega_\phi = 50.0$ rad/s. As shown in Fig. 11, in the case using $\Delta t = 0.050$ to 0.10 sec, more than 10 nonlinear iterations are required to obtain a converged solution. Moreover, in the case using $\Delta t > 0.1$ sec, the iterations failed to converge. On the other hand, the nonlinear iterations are converged in the case using $\Delta t < 0.005$ sec. Therefore, Δt is fixed at 0.005 sec.
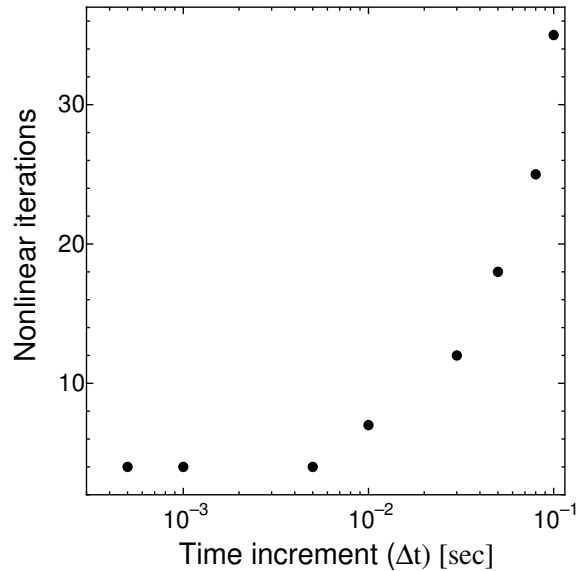

Fig. 11. Relation between the time increment Δt vs the number of nonlinear iterations at the time $t = 10$ sec.

(a) $\omega_\phi = 2.00$ rad/s

(b) $\omega_\phi = 5.00$ rad/s

(c) $\omega_\phi = 50.50$ rad/s
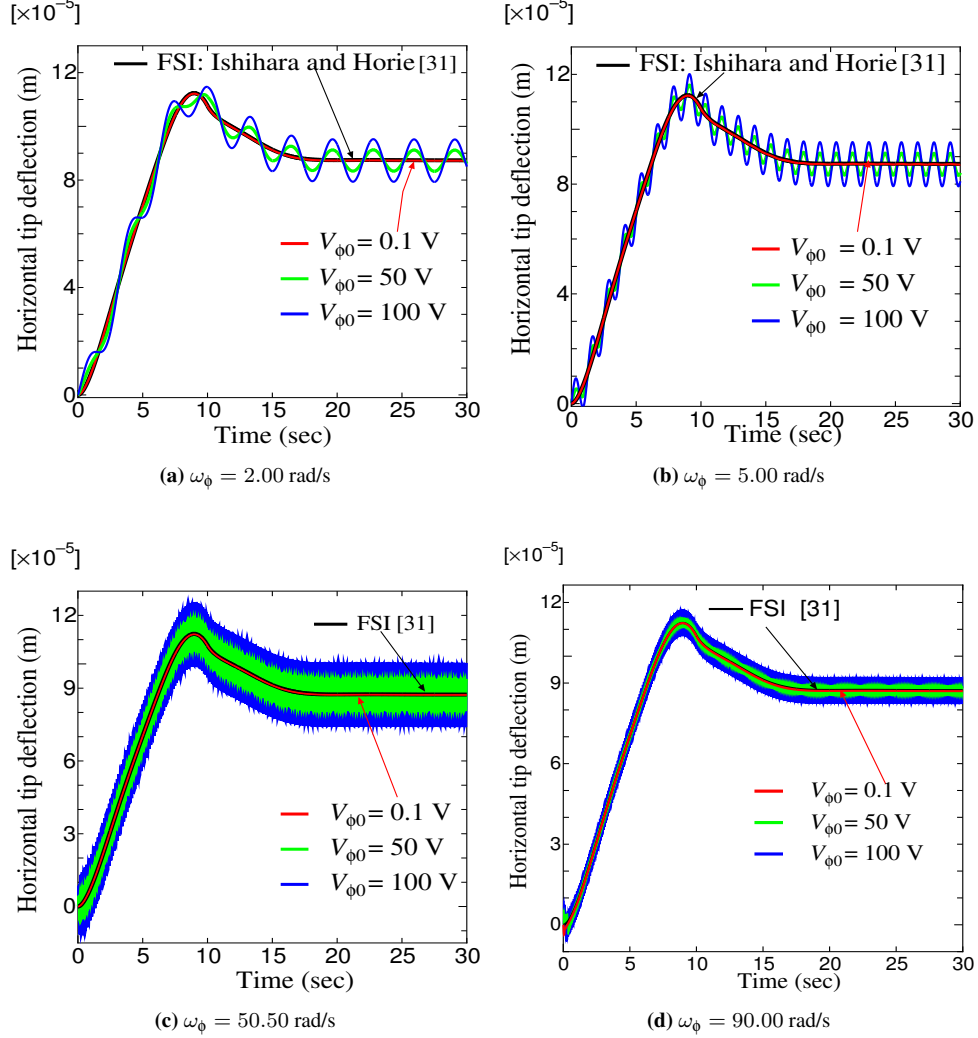
(d) $\omega_\phi = 90.00$ rad/s

Fig. 12. Tip horizontal displacement of the PVDF bimorph actuator in converging channel (with fluid bc's $\frac{V_{max}}{2}(1 - \cos\frac{\pi t}{10})$) for an applied AC voltage $V_\phi = V_{\phi 0}\sin\omega_\phi t$ at various input voltage frequency ω_ϕ and various bias voltage $V_{\phi 0}$ analyzed using unified BGS and N-R loop approach.

Now the piezoelectric-structure-fluid interaction analysis results for the actuator setup shown in Fig. 7(a) is presented. Since the FSI benchmark problem has no analytical solution or experimental data, a reference FSI solution obtained using Ishihara and Horie [31] was taken as the exact solution for PVDF/PZT-5H material instead of rubber in silicone oil. Piezoelectric bimorph actuator layers are polarized opposite to each other. The time increment Δt is fixed to 0.005 sec. Fig. 12 shows the vibration characteristics of the tip of the bimorph actuator in response to various input AC signals with different input voltage frequencies. One can see in Fig. 12 that, the response for input voltage $V_{\phi_0} = 0.1$ volt with frequencies $\omega_\phi = 2.0, 5.0, 50.50$ and 90.0 rad/s, the curve coincides with that of the reference solution [31]. This indicates that the piezoelectric
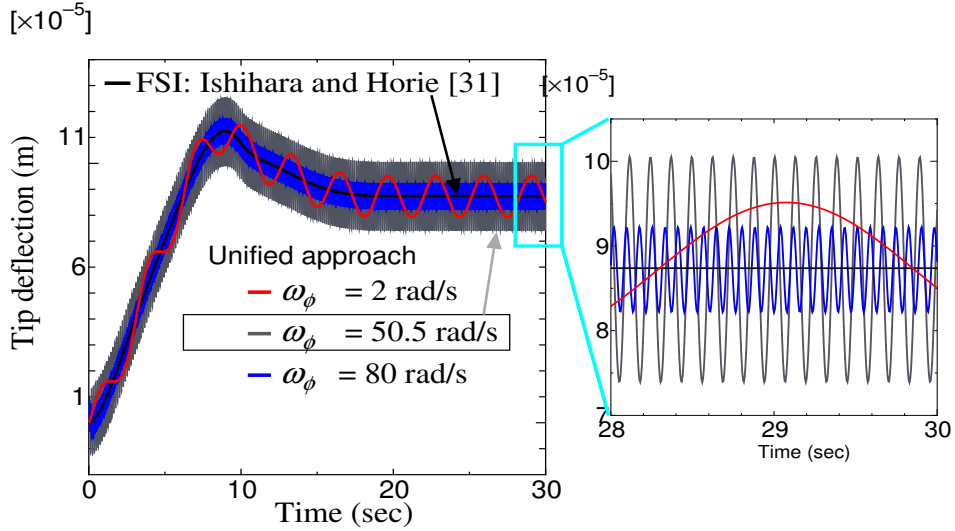
24

Fig. 13. AC response of PVDF piezoelectric bimorph actuator in converging fluid channel at $V_{\phi0} = 100$V, $V_{in} = 0.06067$ m/s and $f = 0.05$Hz ($v_{in} = \frac{V_{max}}{2}(1 - \cos\frac{\pi t}{10})$).

and inverse-piezoelectric effect at $V_{\phi_0} = 0.1$V is negligible. The shape of the present piezoelectric field–structure–fluid interaction curve at $V_{\phi_0} = 0.1$V is identical to those from the numerical solutions of Mok et al. [33], Neumann et al. [41], and Ishihara and Horie [31]. As the input voltage is increased, the coupling becomes significantly strong and increases the induced electric force. Therefore, harmonic oscillations occur around the reference solution, as shown in Fig. 12 for $V_{\phi_0} = 50$ and 100 volt. As shown in the enlarged view graph of Fig. 13, it is clear that the average behavior of the obtained solution at $V_{\phi_0} = 100$V coincides with the reference solution in the quasi–state phase.

Fig. 13 shows the frequency response of the bimorph actuator (case 1) in the converging channel for the imposed fluid velocity boundary conditions at a bias voltage $V_{\phi_0} = 100$V for various input voltage frequency ω_ϕ. From Fig. 13, it is evident that the harmonic oscillations for $\omega_\phi = 2.0$ rad/s, 50.5 rad/s, 80.0 rad/s are about the reference FSI solution for all the input voltage frequency. Also, the response in $\omega_\phi = 50.5$ rad/s achieved the largest peak amplitude among the different input voltage frequencies, indicating the resonance at this voltage frequency.

In general, the resonance frequency of the piezoelectric bimorph actuator is the same as the beam resonance. To validate the frequency response of the bimorph actuator in the fluid, we use the pure FSI setup shown in Fig. 7(b) and compare with the results obtained for the actuator problem setup shown in Fig. 7(a). In Fig. 14(a), the blue curve shows the summary of the maximum horizontal tip displacement of PVDF bimorph actuator versus input voltage frequency for the problem setup given in Fig. 7(a) and similarly the black curve shows the frequency response of the elastic body with structural properties of PVDF material versus the input frequency of an equivalent external mechanical force for the problem setup given in Fig. 7(b). As shown in the Fig. 14, the actuator setup shows the resonance when the input voltage frequency $\omega_\phi = 50.50$ rad/s, while the pure FSI setup shows the resonance when the input frequency of the equivalent external mechanical force $\omega = 50.90$ rad/s. Both the solution is very close to that of the theo-

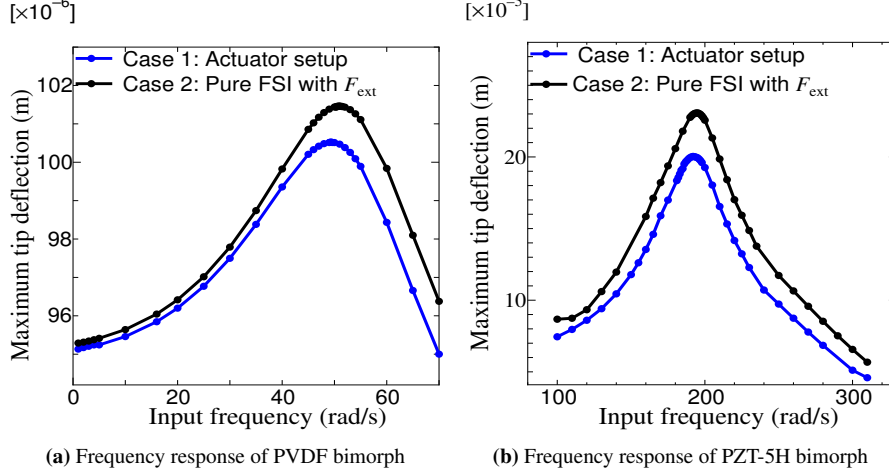**(a)** Frequency response of PVDF bimorph   **(b)** Frequency response of PZT-5H bimorph

Fig. 14. Frequency response curve of a piezoelectric bimorph actuator in converging fluid channel at $V_{\phi 0} = 100$V, V_{in} = 0.06067 m/s and $f = 0.05$Hz ($v_{in} = \frac{V_{max}}{2}(1 - \cos\frac{\pi t}{10})$) and pure FSI with external mechanical force at the tip with $V_{\max} = 0.06067$ m/s and $f = 0.05$Hz ($v_{in} = \frac{V_{max}}{2}(1 - \cos\frac{\pi t}{10})$).

retical solution $\omega_{\text{fld}}^{(1)} = 52.45$ rad/s using Eq.(62). Fig. 14(b) shows the frequency response of PZT-5H actuator for case 1 and case 2. The PZT-5H bimorph shows resonance when the input voltage frequency is $\omega_\phi = 192.0$ rad/s for both actuator setup and pure FSI setup. The theoretical solution for the PZT-5H bimorph in fluid is $\omega_{\text{fld}}^{(1)} = 198.69$ rad/s using Eq.(62). Their relative error is 3.3%. This indicates that the proposed method accurately captures the AC response of the piezoelectric bimorph actuator in the fluid. As shown in Fig. 14, the vibration amplitude in the actuator setup decreases a bit compared with the pure FSI case. This is because of the inverse piezoelectric effect counterplays with the mechanical vibration, as discussed in Ref.[51]. The vibration amplitude decrease in the PVDF bimorph actuator problem (case 1) shows similarities with the results presented by Song et al. [51]. Also, this amplitude decrease in the actuator setup compared with the pure FSI can be understood as the equivalent external resistance of the inverse piezoelectric effect with optimum resistance value due to the applied electrical potentials onto the piezoelectric bimorph layers [52, 53].

Figs. 15(a) and 15(b) show the frequency response of the PVDF and PZT-5H bimorph open and short-circuit sensor configuration for the problem setup given in Fig. 7(c) and (d), respectively. It is known that the resonance frequency of the piezoelectric bimorph beam under closed circuit and the open circuit configuration are co-related as [51, 54]

$$f_{short} = f_{open}\sqrt{1 - k_{31}^2}, \tag{63}$$

where k_{31} is the electro-mechanical coupling factor of a piezoelectric material, f_{short} is the resonance frequency of the piezoelectric bimorph in the closed or short circuit configuration, and f_{open} is the resonance frequency of the open circuit configuration. The value of k_{31} for PVDF is about 0.12, therefore the difference between f_{short} and f_{open} is within 1%. As k_{31} of PZT-5H is about 0.4, the difference between f_{short} and f_{open} is approximately within 10%, as shown in the studies of Zhu et al. [52]. In Fig. 15(a), the shift in the resonance frequencies in PVDF

26

(a) Frequency response of PVDF bimorph sensor   **(b)** Frequency response of PZT-5H bimorph sensor
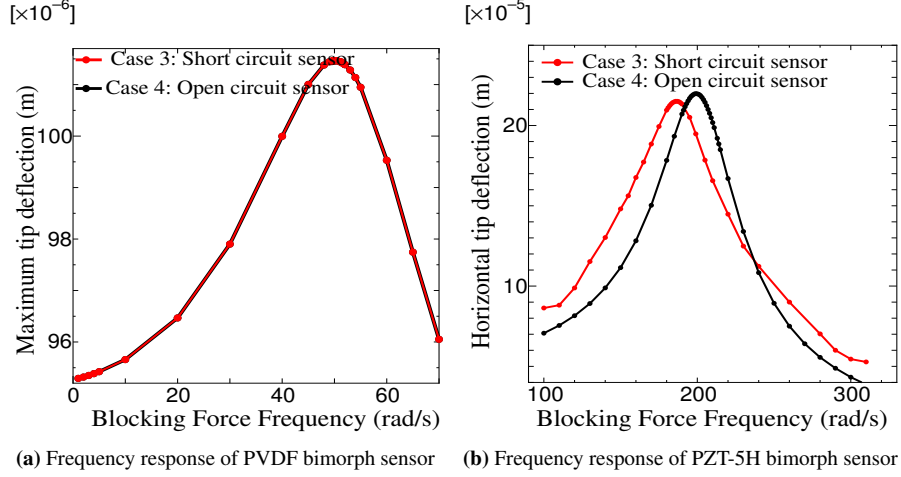
Fig. 15. Frequency response curve of a piezoelectric bimorph sensor configuration.

piezoelectric bimorphs in the open- and closed-circuit configuration are negligible, unlike the case of PZT-5H based piezoelectric bimorphs of which the resonance frequency shows a noticeable shift upon the electric configuration as shown in Fig. 15(b). Song et al. [51] demonstrated through numerical and experimental studies that the frequency shift is negligible between open- and closed-circuit sensor configurations for a piezoelectric bimorph made of PVDF material. The present results follow the same trend with [51] for PVDF piezoelectric bimorph. The PZT-5H bimorph open circuit sensor configuration shows the resonance when the equivalent force frequency is $\omega = 199.0$ rad/s, while the short circuit configuration shows the resonance at the input frequency $\omega = 186.0$ rad/s. The difference between open- and closed-circuit resonance frequency is 6.6%, thus justifying the relation given in Eq.(63) for PZT-5H material. The simulation results in [53] also show a 5% difference between the open- and closed-circuit configurations for the piezoelectric bimorph based on PZT-5H material. Therefore, the simulated results using the proposed algorithm follow the same trends upon the shift in the resonance. The method accurately take into account the AC response of a thin piezoelectric bimorph upon the material type and electrical configuration.

5. Conclusions

A hierarchically decomposed finite element method is proposed for modeling the triply coupled piezoelectric-structure-fluid interaction of a piezoelectric bimorph made of PVDF and PZT-5H materials in the viscous fluid media. In the proposed method, the piezoelectric-structure-fluid interaction system is hierarchically decomposed as follows: The triply coupled system is partitioned into subsystems of piezoelectric field and fluid-structure interaction, then the piezoelectric field and the fluid-structure interaction are strongly coupled using the block Gauss-Seidel method. The fluid-structure interaction subsystem is further decomposed using the projection method, i.e., the FSI is split into the fluid-structure velocity field and the pressure field using an algebraic splitting, and then the structure-fluid velocity field is again partitioned into the structure velocity field and the fluid velocity field using the explicit time integration for the fluid

27

interior DOFs. Two approaches are presented for the management of the block Gauss–Seidel and Newton-Raphson iteration loops and they are studied for the purpose of computational efficiency. In the first approach, the nonlinear N-R loop is placed inside the BGS iteration loop. In this approach, in every BGS iteration, several N-R iterations are executed until the energy tolerance criteria is satisfied. On the other hand, in the second approach, the BGS and N-R loops are unified into a single loop.

The proposed method takes into account the triply coupled interaction phenomena. As a fundamental validation, when the bimorph actuator is excited at very low bias voltage in the fluid channel with the inlet fluid velocity, the horizontal tip displacement of the bimorph actuator coincides with the reference FSI solutions. At higher bias voltages, harmonic oscillation appears about the reference solution, indicates a strong inverse piezoelectric coupling in the fluid. The unified BGS and N-R loops are efficient than the conventional BGS iteration with the N-R loop since the later requires more number of iterations to satisfy the convergence conditions. However, both approaches show the same level of solution accuracy.

In the actuator mode, the resonance frequency of a thin flexible piezoelectric bimorph in the fluid agrees well with the theoretical solutions. Also, in the sensor mode, the shift in the resonance frequency upon the electric boundary conditions is matched well with the theoretical approximations. It is shown that the resonance frequency difference between the open- and closed-circuit sensor electric configurations in PVDF piezoelectric bimorphs has a negligible shift. However, a noticeably shift upon the electric boundary conditions can be seen in PZT5H piezoelectric bimorphs. The simulated frequency responses and vibration amplitudes of the thin flexible piezoelectric bimorphs analyzed using the proposed method shows a good agreement with the previous studies.

Acknowledgments

References

[1] J.R. Bronson, J.S. Pulskamp, R.G. Polcawich, C.M. Kroninger, E.D. Wetzel, Pzt mems actuated flapping wings for insect-inspired robotics, IEEE International Conference on Microelectromechanical systems, (2009) 1047–1050 doi:10.1109/MEMSYS.2009.4805566.

[2] D. Ishihara, N. Ohira, M. Takagi, T. Horie, Fluid-structure interaction design of insect-like micro flapping wing, Proc of the VVII International Conference on Computational Methods for Coupled Problems in Science and Engineering, European Community on Computational Methods in Applied Sciences, Rhodes Island, (2017) 870–875.

[3] Y. Tanaka, T. Oko. H. Mutsuda, A.A. Popov, R. Patel, S.M. William, Forced vibration experiments on flexible piezoelectric devices operating in air and water environments, International Journal of Applied Electromagnetics and Mechanics, **45** (2014) 573–580. doi:10.3233/JAE-141879.

[4] Y. Tanaka, T. Oko. H. Mutsuda, R. Patel, S.M. William, A.A. Popov, An experimental study of wave power generation using a flexible piezoelectric devices, Journal of Ocean and Wind Energy, **2** (2015) 28–36.

[5] S. Ravi, A. Zilian, Numerical modeling of flow driven piezoelectric energy, Computational Methods for Solids and Fluids:Springer International Publishing, **41** (2016) 399–426. doi:10.1007/978-3-319-27996-1_15.

[6] S. Kaneko , G. Hong, N. Mitsume, T. Yamada, S. Yoshimura, Numerical study of active control by piezoelectric materials for fluid–structure interaction problems, Journal of Sound and Vibration, **435** (2018) 23–35. doi:10.1016/j.jsv.2018.07.044.

[7] H. Allik, T.J.R. Hughes, Finite element method for piezoelectric vibration, International Journal for Numerical Methods in Engineering, **2** (1970) 151–157. doi:10.1002/nme.1620020202.

[8] Z. Wang, S. Chen, W. Han, The static shape control for intelligent structures, Finite Elements in Analysis & Design, **26** (4) (1997) 303–314. doi:10.1016/S0168-874X(97)00086-3.

[9] J. Fish, W. Chen, Modeling and simulation of piezocomposites, Computer Methods in Applied Mechanics and Engineering, **192** (2003) 3211 – 3232. `doi:10.1016/S0045-7825(03)00343-8`.

[10] Q. Zhang, T. Hisada, Analysis of fluid–structure interaction problems with structural buckling and large domain changes by ale finite element method, Computer Methods in Applied Mechanics and Engineering, **190** (2001) 6341–6357. `doi:10.1016/S0045-7825(01)00231-6`.

[11] B. Hubner, E. Walhorn, D. Dinkler, A monolithic approach to fluid–structure interaction using space–time finite elements, Computer Methods in Applied Mechanics and Engineering, **193** (2004) 2087–2104. `doi:10.1016/j.cma.2004.01.024`.

[12] D.Ishihara, S. Yoshimura, A monolithic approach for interaction of incompressible viscous fluid and an elastic body based on fluid pressure poisson equation, International Journal for Numerical Methods in Engineering, **64** (2015) 167–203. `doi:10.1002/nme.1348`.

[13] P. Gaudenzi, K.J. Bathe, An iterative finite element procedure for the analysis of piezoelectric continua, Journal of Intelligent Material Systems and Structures **6** (1995) 226–273. `doi:10.1177/1045389X9500600213`.

[14] P.C. Ramegowda, D. Ishihara, T. Niho, T. Horie, Performance evaluation of numerical finite element coupled algorithms for structure–electric interaction analysis of mems piezoelectric actuator, International Journal of Computational Methods **16**(7) (2019) 1850106. `doi:10.1142/S0219876218501062`.

[15] P.C. Ramegowda, D. Ishihara, T. Niho, T. Horie, A novel coupling algorithm for the electric field–structure interaction using a transformation method between solid and shell elements in a thin piezoelectric bimorph plate analysis, Finite Elements in Analysis and Design **159** (2019) 33–49. `doi:10.1016/j.finel.2019.02.001`.

[16] P.C. Ramegowda, D. Ishihara, R. Takata, T. Niho, T. Horie, Finite element analysis of thin piezoelectric bimorph with a metal shim using solid direct-piezoelectric and shell-inverse piezoelectric coupling with pseudo-piezoelectric evaluation, Composite Structures ,under review.

[17] R. Takata,D.Ishihara, P.C. Ramegowda, T. Niho, T. Horie, Solid piezoelectric - shell inverse piezoelectric partitioned analysis method for thin piezoelectric bimorph with conductor layers, Transactions of the Japan Society for Computational Engineering and Science **2019** (2019) 20190011. `doi:10.11421/jsces.2019.20190011`.

[18] S. Minami, S. Yoshimura, Performance evaluation of nonlinear algorithms with line search for partitioned coupling technique for fluid–structure interactions, International Journal for Numerical Methods in Fluids **64** (2010) 1129–1147. `doi:10.1002/fld.2274`.

[19] T. Yamada, S. Yoshimura, Line search partitioned approach for fluid–structure interaction analysis of flapping wing, Computer Modeling in Engineering and Science **24** (2008) 51–60. `doi:10.3970/cmes.2008.024.051`.

[20] S. Badia, F. Nobile, C. Vergara, Fluidstructure partitioned procedures based on robin transmission conditions, Journal of Computational Physics **227** (2008) 7027–7051. `doi:10.1016/j.jcp.2008.04.006`.

[21] S. Rugonyi, K.J. Bathe, On finite element analysis of fluid flows fully coupled with structural interaction, Computer Modeling in Engineering and Science **2** (2001) 195–212. `doi:10.1016/S0045-7949(99)00042-5`.

[22] V. Rochus, S. Gutschmidt, A. Cardona, C. Geuzaine, Electro-mechano-fluidic modeling of microsystems using finite elements, IEEE Transactions on Magnetics **48** (2012) 355–358. `doi:10.1109/TMAG.2011.2173663`.

[23] S.K. De, N. R. Aluru, Coupling of hierarchical fluid models with electrostatic and mechanical models for the dynamic analysis of mems, Journal for Micromechanics and Microengineering **16** (2006) 1705–1719. `doi:0.1088/0960-1317/16/8/036`.

[24] R. Ghosh, S. Mukherjee, Fully lagrangian modeling of dynamics of mems with thin beams–part ii: Damped vibrations, Journal of Applied Mechanics **76** (2009) 051008. `doi:10.1115/1.3086786`.

[25] D. Ishihara, T. Horie, T. Niho, T. Baba, Hierarchal decomposition for the structure-fluid-electrostatic interaction in a microelectromechanical system, Computer Modeling in Engineering and Sciences **108** (2015) 429–452.

[26] M. Raulli, K. Maute, Optimization of fully coupled electrostatic–fluid–structure interaction problems, Computers & Structures **83** (2005) 221–233. `doi:10.1016/j.compstruc.2004.08.003`.

[27] J.H. Kim, H.S. Kim, Finite element analysis of piezoelectric underwater transducers for acoustic characteristics, Journal of Mechanical Science and Technology **23** (2009) 452–460. `doi:10.1007/s12206-008-1126-x`.

[28] Y. Amini, H. Emdad, M. Farid, Fluid–structure interaction analysis of a piezoelectric flexible plate in a cavity filled with fluid, Scientia Iranica B **23** (2016) 559–565. `doi:10.24200/sci.2016.3843`.

[29] K.J. Bathe, H. Zhang, Y. Yan, The solution of maxwells equations in multiphysics, Computers & Structures **132** (2014) 99–112. `doi:10.1016/j.compstruc.2013.09.006`.

[30] A. Benjeddou, Advances in piezoelectric finite element modeling of adaptive structural elements: a survey, Computers & Structures **76** (2000) 347–363. `doi:10.1016/S0045-7949(99)00151-0`.

[31] D.Ishihara, T. Horie, A projection method for the monolithic interaction system of an incompressible fluid and a structure using a new algebraic splitting, Computer Modeling in Engineering and Sciences **101** (2014) 421–440. `doi:10.3970/cmes.2014.101.421`.

[32] T. Nomura, T.J.R. Hughes, An arbitrary lagrangian–eulerian finite element formulation for interaction of fluid and a rigid body, Computer Methods in Applied Mechanics and Engineering; **95** (1992) 115–138. `doi:10.1016/0045-7825(92)90085-X`.

[33] Mok, D. P.; Wall, W. A., Partitioned analysis schemes for the transient interaction of incompressible flows and nonlinear flexible structures, Trends in Computational Structural Mechanics. CIMNE: Barcelona (2001) 689–698.

[34] T.E. Tezduyar, S. Mittal, S. Ray, R. Shih, Incompressible flow computations with stabilized bilinear and linear equal-order-interpolation velocity-pressure elements, Computer Methods in Applied Mechanics and Engineering **95** (1992) 221–242. `doi:10.1016/0045-7825(92)90141-6`.

[35] TA. Brooks, T.J.R. Hughes, Streamline upwind/petrovgalerkin formulations for convection dominated flows with particular emphasis on the incompressible navierstokes equation, Computer Methods in Applied Mechanics and Engineering **32** (1982) 199–259. `doi:10.1016/0045-7825(82)90071-8`.

[36] T. E. Tezduyar, Stabilized finite element formulations for incompressible flow computations, Advances in Applied Mechanics **28** (1992) 1–44. `doi:10.1016/S0065-2156(08)70153-4`.

[37] S. Rugonyi, K.J. Bathe, On finite element analysis of fluid flows fully coupled with structural interactions, Computer Modeling in Engineering and Science **2** (2004) 195–212. `doi:10.3970/cmes.2001.002.195`.

[38] D. Ishihara, Role of fluid–structure interaction in generating the characteristic tip path of a flapping flexible wing, Physical Review E **98** (2018) 032411, 19 pages. `doi:10.1103/PhysRevE.98.032411`.

[39] K.J. Bathe, A.P. Cimento, Some practical procedures for the solution of nonlinear finite element equations, Computer Methods in Applied Mechanics and Engineering **22** (1980) 59–85. `doi:10.1016/0045-7825(80)90051-1`.

[40] E.N. Dvorkin, K.J. Bathe, A continuum mechanics based four-node shell element for general nonlinear analysis, Engineering Computation **1** (1984) 77–88. `doi:10.1108/eb023562`.

[41] M. Neumann, S.R. Tiyyagura, W.A. Wall, Robustness and efficiency aspects for computational fluid structure interaction, Computational Science and High Performance Computing II **91** (2006) 99–114. `doi:10.1007/3-540-31768-6_9`.

[42] S.R. Idelsohn, F. Del Pin, R. Rossi, E. Onate, Fluid-structure interaction problems with strong added-mass effect, International Journal for Numerical Methods in Engineering **80** (2009) 1261–1294. `doi:10.1002/nme.2659`.

[43] J. Degroote, K.J. Bathe, J. Vierendeels, Performance of a new partitioned procedure versus a monolithic procedure in fluidstructure interaction, Computer & Structures; **87** (2009) 793–801. `doi:10.1016/j.compstruc.2008.11.013`.

[44] Y. Carretta, R. Boman, J. Bech, N. Legrand , M. Laugier, J.P. Ponthot, Numerical modelling of microscopic lubricant flow in sheet metal forming. application to plane strip drawing, International Journal for Numerical Methods in Engineering **112** (2017) 203–237. `doi:10.1002/nme.5509`.

[45] Q.M. Wang, L.E. Cross, Performance analysis of piezoelectric cantilever bending actuator, Ferroelectrics **215** (1998) 187–213. `doi:10.1080/00150199808229562`.

[46] H. Noguchi, T. Hisada, Sensitivity analysis in post buckling problems of shell structures, Computers & Structures **47** (1993) 699–710. `doi:10.1016/0045-7949(93)90352-E`.

[47] C.A.Van Eysden, J.E. Sader, Resonance frequencies of a cantilever beam immersed in a fluid, Journal of Applied Physics **100** (2006) 114916, 8 pages. `doi:10.1063/1.2401053`.

[48] T. Cai, Theoretical analysis of torsionally vibrating microcantilevers for chemical sensor applications in viscous liquids, Ph.D Dissertation, Marquette University.

[49] S. Zhu, B. Jiang, W. Cao, Characterization of piezoelectric materials using ultrasonic and resonant techniques, Proceeding of SPIE, Medical Imaging:Ultrasonic Transducer Engineering **3341** (1998) 154–162. `doi:10.1117/12.307996`.

[50] D.Ishihara, S. Kanei, S. Yoshimura, T. Horie, Efficient parallel analysis of shell-fluid interaction problem by using monolithic method based on consistent pressure poisson equation, Journal of Computational Science and Technology **2** (2008) 185–196. `doi:10.1299/jcst.2.185`.

[51] J. Song, G. Zhao, B. Li, J. Wang, Design optimization of pvdf–based piezoelectric energy harvesters, Heliyon; **3** (2017) e00377, 18 pages. `doi:10.1016/j.heliyon.2017.e00377`.

[52] M. Zhu, E. Worthington, J. Njuguna, Analysis of power output of piezoelectric energy harvesting devices directly connected to a resistive load using a coupled piezoelectric circuit finite element method, IEEE Transactions on Ultrasonics, Ferroelectrics, and Frequency Control **56** (2009) 1309–1317. `doi:10.1109/TUFFC.2009.1187`.

[53] M. Zhu, E. Worthington, A. Tiwari, Design study of piezoelectric energy harvesting devices for generation of higher electrical power using a coupled piezoelectric–circuit finite element method, IEEE Transactions on Ultrasonics, Ferroelectrics, and Frequency Control **57** (2010) 427–437. `doi:10.1016/j.sna.2017.07.009`.

[54] M. Renaud, R. Elfrink, M. Jambunathan, C. de Nooijier, Z. Wang, M. Rovers, R. Vullers, R. V. Schaijk, Optimum power and efficiency of piezoelectric vibration energy harvesters with sinusoidal and random vibrations, Journal of Micromachanics and Microengineering **22** (2012) 105030. `doi:0.1088/0960-1317/22/10/105030`.